NOVA SCHOOL OF SCIENCE & TECHNOLOGY

DEPARTMENT OF MATERIALS SCIENCE

EVA JESUS MARQUES ALMEIDA

BSc in Micro and Nanotechnologies Engineering

STRUCTURAL COLOUR APPLICATION IN PHOTONIC ENHANCED PEROVSKITE SOLAR CELLS FOR BIPV

MASTER IN MICRO AND NANOTECHNOLOGIES ENGINEERING

NOVA University Lisbon
October, 2023

NOVA SCHOOL OF
SCIENCE & TECHNOLOGY

DEPARTMENT OF
MATERIALS SCIENCE

STRUCTURAL COLOUR APPLICATION IN PHOTONIC ENHANCED PEROVSKITE SOLAR CELLS FOR BIPV

EVA JESUS MARQUES ALMEIDA

BSc in Micro and Nanotechnologies Engineering

Adviser: Manuel Mendes
Assistant Professor, NOVA University Lisbon

Co-adviser: Hugo Águas
Associate Professor, NOVA University Lisbon

Examination Committee

Chair: Rodrigo Ferrão de Paiva Martins
Full Professor, NOVA University Lisbon

Rapporteur: Matthias Auf der Maur
Researcher, Tor Vergata University of Rome

Adviser: Manuel Mendes
Assistant Professor, NOVA University Lisbon

MASTER IN MICRO AND NANOTECHNOLOGIES ENGINEERING

NOVA University Lisbon
October, 2023

Structural colour application in photonic enhanced Perovskite Solar Cells for BIPV

Copyright © Eva Jesus Marques Almeida, NOVA School of Science and Technology, NOVA University Lisbon.
The NOVA School of Science and Technology and the NOVA University Lisbon have the right, perpetual and without geographical boundaries, to file and publish this dissertation through printed copies reproduced on paper or on digital form, or by any other means known or that may be invented, and to disseminate through scientific repositories and admit its copying and distribution for non-commercial, educational or research purposes, as long as credit is given to the author and editor.

This document was created with the (pdf/Xe/Lua)LaTeX processor and the NOVAthesis template (v7.0.3) [1].

Acknowledgements

Firstly, I want to acknowledge Professor Elvira Fortunato and Professor Rodrigo Martins, for providing all the necessary resources for this project to be executed. I thank my advisers, Professor Manuel Mendes and Professor Hugo Águas, for giving me the opportunity to be involved in this project and for meeting all the hardships with attentiveness.

Above all, I would like to express my gratitude to my mentor, Miguel Alexandre, for the guidance and advices that helped me grow. To everyone in the PV team, I appreciate all the attention and constructive criticism throughout the last months, with special mentions to Ivan Santos.

Agradeço aos meus pais, por apoiarem as minhas ambições e serem os meus maiores admiradores. À Alice, por todos os momentos felizes, por ser o motivo pelo qual eu luto por um futuro melhor. À minha irmã, a quem devo a maior admiração, por ser a inspiração e guia da minha vida.

Lastly, I thank everyone, friends and colleagues, who have helped and supported me, academically and personally, during the past 5 years. To Gonçalo, I could not have finished this journey without your company, you have been my best friend during the worst moments and will forever be the partner of a lifetime. Rafael Loução, I will never forget all the midnight oil burning study seasons and last-minute revisions/panic attacks. Ucais, thank you for receiving me with open arms in all the insightful meals of the past months.

”

“And we forgot the taste of bread, the sound of trees, the softness of the wind. We even forgot our own name.”

— Gollum, "The Lord of the Rings"

Abstract

The current unsustainable energy consumption of society has increased the demand for clean and virtually unlimited energy sources, such as solar energy. In the market of solar electricity, building integrated photovoltaics (BIPV) has been receiving considerable attention. For this application, the compatibility of photovoltaic modules with construction materials requires the development of flexible, low-weight, thin-film solar cells. $MAPbI_3$ solar cells (1.55 eV bandgap) with light trapping (LT) structures were chosen for this study, as these have excelled at maintaining high optical performance, despite low cell thickness.

A particularity of the BIPV industry is that, unlike most photovoltaic studies, the aesthetics related to the colours of the building material are valued. Thus, this work developed a computational method that designs solar cells with LT features capable of increasing both the optical performance and the solar cell affinity to a specific colour. The focus was then to study how the geometrical features of solar cells and respective LTs affect the colour and optical properties, as well as their layout optimization and angular sensitivity. Here we specifically addressed magenta and green chromaticity since these cover the reflection peaks of the primary colours in the RGB system, and are generally some of the hardest colorations to obtain for high-performance solar cells.

A variety of LTs were designed, simulated and optimized, from simple gratings to complex semi-spheroids. The maximum current density values were obtained for solar cells with top dome structures — 22.07 mA/cm^2 for magenta and 21.40 mA/cm^2 for green — reaching an increase of 6.68% and 3.44%, respectively, relative to the reference cell in planar configuration. Regarding angular homogeneity, this work tested incidence angles between 0° and 60°, where, at the highest illumination angle, a maximum current density of J_{SC} = 20.85 mA/cm^2 was obtained, for magenta domes, corresponding to a relative J_{SC} loss of 5.53%.

Keywords: Building integrated photovoltaics, Perovskite solar cell, Light trapping, Structural colour, FDTD optimization

Resumo

O atual consumo de energia insustentável aumentou a procura de fontes de energia limpa ilimitadas, como a energia solar. No mercado de eletricidade solar, fotovoltaicos integrados em edifícios (BIPV) têm recebido considerável atenção. A compatibilidade dos módulos fotovoltaicos com os materiais de construção requer o desenvolvimento de células solares de filme fino, flexíveis e de baixo peso. Células de $MAPbI_3$, (*bandgap* 1.55 eV) com estruturas de captura de luz (LT) foram escolhidas para este estudo, devido às suas excelentes propriedades óticas, apesar da baixa espessura da célula.

Uma particularidade desta indústria é o valor estético da cor dos materiais de construção, algo raramente considerado em estudos fotovoltaicos. Nesse sentido, este trabalho desenvolveu um método computacional que concebe células solares com estruturas LT, responsáveis por aumentar a performance ótica e pela reflexão de uma cor específica na célula solar. Este estudo focou-se no modo como as características geométricas das células solares e LTs afetam a cor e as propriedades ópticas, bem como na otimização dos layouts e sensibilidade angular. Aqui abordamos especificamente as cromaticidades magenta e verde, uma vez que estas cobrem a reflexão das cores primárias no sistema RGB e são, geralmente, das colorações mais difíceis de obter para células solares de alto desempenho.

Uma variedade de LTs foram projetados, simulados e otimizados, desde *gratings* simples até semiesferóides complexos. Os valores máximos de densidade de corrente foram obtidos em células solares com estruturas em cúpula — 22.07 mA/cm^2 para magenta e 21.40 mA/cm^2 para verde — atingindo um aumento de 6,68% e 3,44%, respectivamente, em relação à célula plana de referência. Relativamente à homogeneidade angular, este trabalho testou ângulos de incidência entre 0° e 60°, onde, no maior ângulo, uma densidade máxima de corrente de 20.85 mA/cm^2 foi obtida para cúpulas magenta, correspondendo a uma perda relativa J_{SC} de 5,53%.

Palavras-chave: Fotovoltaicos integrados em edifícios, Célula solar de perovskite, Captura de luz, Cor estrutural, Otimização FDTD

Motivation

The increasingly concerning topic of fossil fuel energy crisis is stimulating the renewable energy sector to develop new methods of capturing energy available in nature. Within this branch, solar energy is growing into a popular alternative to non-renewable fuels, due to its wide availability, corresponding to 4.5% of total global electricity generation and resulting in the fastest growing renewable energy in the year 2022 [2]. This has been leading to an advancement in building integrated photovoltaics (BIPV), which consist of photovoltaic modules as part of the outward structures of buildings, allowing for better exploration of solar energy.

The BIPV market was valued at $14.0 billion in 2020, and is projected to increase to $86.7 billion by 2030, with a variety of applications – roofs, façades, walls and semi-transparent glass (seen in Figure 1) – indicating how fast this technology is estimated to grow [3]. A section of BIPV technologies require the implementation of durable, aesthetically pleasing, flexible thin-film solar cells, with elevated standards concerning energy conversion efficiency. To this end, and seeing as regular solar cells usually present dark colors (for maximum light absorption), BIPVs encounter a setback, as the construction industry demands mostly coloured materials, for visual appeal. However, designing coloured solar cells implies the reflection of a portion of the solar spectrum, that could otherwise be used for energy production, resulting in lower efficiencies and J_{SC}.

Various studies have worked to mitigate this effect, by employing light management techniques that seek to manipulate the interference of light, in order to generate a certain colour whilst improving the cell's optical properties [4]. Similarly, the work presented in this thesis aims to demonstrate how light trapping (LT) features may be a solution to the setbacks of these technologies, as different structures can enhance the scattering phenomenon and increase the light's optical path in the thin absorbing layer, and generate a variety of structural colours by optimization of the cells' geometrical attributes. Considering all these factors, there is an interest in developing a computational method capable of optimizing any solar cell layout to reflect a selected colour for maximum photocurrent generation, thus seizing the most solar power out of coloured cells.

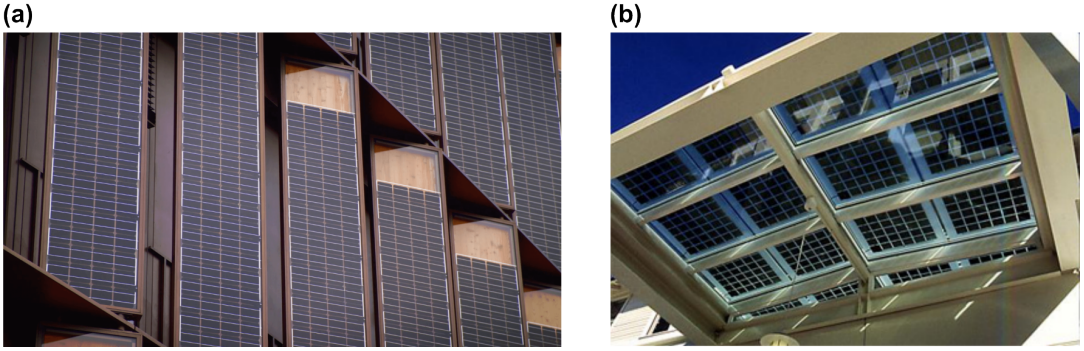


Figura 1: (a) Photovoltaic modules integrated as shading grates into the façade of the town hall in Stühlinger, Freiburg (adapted from [5]). (b) A photovoltaic skylight entryway (adapted from [6]).

Contents

Motivation vii

List of Figures x

List of Tables xiv

Acronyms xv

Symbols xvi

1 Introduction 1
- 1.1 Perovskite solar cells (PSCs) . . . 1
- 1.2 Light trapping features . . . 2
- 1.3 Structural colour . . . 3

2 Simulation methods and setup 6
- 2.1 Simulation of photonic devices: *Ansys Lumerical*™ FDTD . . . 6
  - 2.1.1 Simulation layout and setup . . . 6
- 2.2 Colour and optical optimization . . . 8
  - 2.2.1 Particle swarm optimization . . . 8
  - 2.2.2 Figure of merit . . . 9

3 Results and analysis 12
- 3.1 Reference cell . . . 12
- 3.2 Photonic structures . . . 13
  - 3.2.1 Screening photonic shape and array symmetry . . . 13
  - 3.2.2 Analysing photonic geometries . . . 15
- 3.3 Optimization process . . . 17
  - 3.3.1 Figure of merit analysis . . . 17
  - 3.3.2 Optimization results: planar solar cells . . . 20
  - 3.3.3 Optimization results: crossed gratings . . . 21
  - 3.3.4 Optimization results: domes . . . 25
  - 3.3.5 Optimization results: overlook . . . 26
- 3.4 Angular uniformity . . . 29

4 Conclusion and future perspectives 32

Bibliography 34

Appendices

A FDTD setup and convergence tests 38

A.1 Convergence test: FDTD simulations at normal angle of illumination . . 39
A.2 Convergence test: FDTD simulations at oblique angles of illumination . 40

B Optimization results: grid plots **44**
B.1 Reference cell 44
B.2 Circle nanopillars 44
B.3 Linear gratings 47

Annexes

I Material data **49**

II FDTD physics solver **50**

III CIE colour system **53**

List of Figures

1 (a) Photovoltaic modules integrated as shading grates into the façade of the town hall in Stühlinger, Freiburg (adapted from [5]). (b) A photovoltaic skylight entryway (adapted from [6]). vii

1.1 (a) Unit cell for the basic ABX_3 halide perovskite structure. Each colour represents different ions: A is the monovalent organic or inorganic cation, B is the divalent metal cation and X is the monovalent halogen anion. (b) Light trapping effect on void-shaped ITO and TiO_2 layers: the red markers in the Perovskite layer represent high absorption zones, due to the near-field forward scattering process promoted by the photonic structures (adapted from [9]). 1

1.2 (a) Schematic of structural colour generation and respective dependence on geometrical features: different grating sizes result in distinct combinations of light interferences and colours. (b) Illustration of the optical loss associated to colour generation (adapted from [20]). 4

2.1 Schematics of the photonic structures analysed in this work and cell layout, with respective geometrical variables. 7

2.2 Particle Swarm Optimization flowchart – progression of the position and velocity of each particle. 10

2.3 Scheme of the method employed in this work and the cycling process that includes finite difference time domain (FDTD) simulations (more thoroughly explained in Section 2.1), reflection/colour conversion (Annex III) and the optimization of the geometrical features of the cells (Section 2.2.1). 11

3.1 Chromaticity and photocurrent density of the flat cell, for a variety of ITO and Spiro-OMeTAD layer thicknesses. 12

3.2 Chromaticity for different combinations of structure height and pitch (width fixed at 0.5 and radius at 0.4) and for combinations of pitch and width/radius (pitch set at 500 nm), for circular (top plots) and squared (bottom plots) nanopillars. 14

3.3 Chromaticity and current density for a range of structure heights and volume ratios occupied by the photonic structures, for different layouts of circular nanopillars and domes: (a), (c) hexagonal and (b), (d) squared symmetries. Pitch was fixed at 500 nm for all structures, and planar ITO layer fixed at 50 nm. 14

3.4 Chromaticity and photocurrent density spectra for different combinations of geometrical parameters, pitch and grating height. 15

3.5 Chromaticity and photocurrent density spectra for different combinations of geometrical parameters, pitch and width/radius. 16

3.6 Search space defined by Equations (2.5) to (2.8), for different combinations of pitch and gratings height of P-polarized magenta solar cells with linear grating LT features. The variables of the functions, red, green and blue (RGB) distance and J_{SC}, are also depicted. For FoM_1 to FoM_3, the colour limit was set to 15. 18

3.7 (a) Progress of figure of method (FoM) and J_{SC} values for 15 particles in the optimizations (50 iterations) of magenta solar cells with linear grating LTs (P-polarized), for a fixed initial seed, using FoM_0 (left column) and FoM_2 (right column, for a colour limit of 15). Each scatter point represents one particle and the corresponding cell colour. (b) Colours at a series of RGB distance (between 0 and 30, calculated by Equation (2.4)) from magenta, $(255, 0, 255)$, and green, $(0, 255, 0)$. 19

3.8 Optimization results for the (a) magenta and (b) green flat cells, for the full optimization range and the zoomed optimization range (light blue marked region). Each profile shows the main optimization variables (ITO and Spiro thicknesses) and the resulting FoM, J_{SC} and Colour Distance for each optimization; the circle-shaped points mark the full-ranged optimization results and the star-shaped points the zoomed optimization results. (c) Reflection spectra of the optimized flat cells for magenta (magenta line), green (green line) and reference cells (dashed line). 22

3.9 Optimization results for magenta solar cells with crossed grating LT features, for the full optimization range and the zoomed optimization range (light blue marked region). Each profile shows the main optimization variables and the resulting FoM, J_{SC} and Colour Distance for each optimization; the circle-shaped points mark the full-ranged optimization results and the star-shaped points mark the zoomed optimization results. 23

3.10 Optimization results for green solar cells with crossed grating LT features, for the full optimization range and the zoomed optimization range (light blue marked region). Each profile shows the main optimization variables and the resulting FoM, J_{SC} and Colour Distance for each optimization; the circle-shaped points mark the full-ranged optimization results and the star-shaped points the zoomed optimization results. . 24

3.11 Reflection spectra of optimal solar cells with crossed grating, with ("Optimized") and without ("w/o LT") photonic structures, for green (left plot) and magenta (right plot), and respective reference spectrum. The solar cell colours were applied to each corresponding lines. 24

3.12 Optimization results for magenta solar cells with domes, for the full optimization range and the zoomed optimization range (light blue marked region). Each profile shows the main optimization variables and the resulting FoM, J_{SC} and Colour Distance for each optimization. 25

3.13 Optimization results for green solar cells with domes, for the full optimization range and the zoomed optimization range (light blue marked region). Each profile shows the main optimization variables and the resulting FoM, J_{SC} and Colour Distance for each optimization. 26

3.14 Reflection spectra of optimal solar cells with domes, with ("Optimized") and without ("w/o LT") photonic features , for green (left plot) and magenta (right plot), and respective reference spectrum. The solar cell colours were applied to each corresponding lines. 26

3.15 (a) Optimal geometry parameters of photonic-enhanced solar cells and (b) corresponding J_{SC}, J_{SC} gain (relative to reference), FoM and RGB distance values. The colours of the markers correspond to the chromaticity of the cell. 27

3.16 Solar cell chromaticity (shown in International Commission on Illumination (CIE) gamut), unpolarized J_{SC} and FoM (shown in polar plots) for the optimal magenta and green cells in planar layout and with the photonic structures (illustrations represented accordingly). The incident angles of illumination (θ) varied between 0° and 60°, with a step of 10°. In the CIE gamuts, the scatter marker size increases along with the angle. 31

A.1 Convergence test results: current density for different mesh configurations, for crossed grating and dome LT structures. 41

A.2 Comparison between the perovskite absorption spectra of the flat cell configuration, obtained by the numeric FDTD method (scatter plots) and by the analytical scattering matrix method (line plots), for 0°, 30° and 60° incident angles of illumination, for P-polarized (TE) and S-polarized (TM) sources. . 43

B.1 Results of the optimization of the flat solar cell for the maximization of J_{SC} (for wide and zoomed variable ranges). 44

B.2 Results of the optimization of magenta solar cells with circular nanopillars LT features: optimal geometrical parameters and respective FoM, J_{SC} and RGB distances for multiple particle swarm algorithm (PSO)s, for wide and zoomed variable ranges. 45

B.3 Results of the optimization of green solar cells with circular nanopillars LT features: optimal geometrical parameters and respective FoM, J_{SC} and RGB distances for multiple PSOs, for wide and zoomed variable ranges. 46

B.4 Reflection spectra attained for optimal solar cells with circular nanopillars, with and without LT features, for green (left plot) and magenta (right plot), and respective reference spectrum. The solar cell colours were applied to each corresponding lines. 46

B.5 Results of the optimization of magenta solar cells with linear gratings LT features: optimal geometrical parameters and respective FoM, J_{SC} and RGB distances for multiple PSOs, for wide and zoomed variable ranges. 47

B.6 Results of the optimization of green solar cells with linear gratings LT features: optimal geometrical parameters and respective FoM, J_{SC} and RGB distances for multiple PSOs, for wide and zoomed variable ranges. 48

B.7 Reflection spectra attained for optimal solar cells with linear gratings, with and without LT features, for green (left plot) and magenta (right plot), and respective reference spectrum. The solar cell colours were applied to each corresponding lines. 48

I.1 Refractive index, real (n) and imaginary (k) components used to simulate the materials in the FDTD solver. Data obtained from [42]. 49

II.1 Propagation of electric (circles) and magnetic (triangles) field nodes throughout space-time. The dashed line divides the nodes between future and past values. Adapted from [43]. 51

II.2 FDTD flowchart - simplification of engine loop iterations, for a system with a source, grid boundaries and non-linear materials. 52

III.1 CIE 1931 colour space: (a) individual response of the 3 types of eye cones, responsible for the perception of wavelengths around blue (S cones), green (M cones) and red (L cones) (adapted from [46]), (b) colour matching functions, (c) chromaticity diagram for various (x, y) coordinates, with respective wavelengths shown around the gamut, in blue (the triangle represents the sRGB area) and (d) MacAdam ellipses, areas where the human eye cannot perceive the different colours (for better visualization, the ellipses are amplified by 10 times). 55

List of Tables

3.1 Variable ranges [bottom limit, top limit] used in the optimization of planar and enhanced solar cells, for magenta and green. 20

3.2 Results of the optimization of planar and structured cells, for magenta $(255, 0, 255)$ and green $(0, 255, 0)$: values of FoM, as defined by Equation (2.7), J_{SC} and respective RGB colours, along with the optimal geometry parameters and corresponding size accurate illustrations (considering a cell base $1\,\mu m^2$), where the thicknesses of the LT, ITO and Spiro layers are represented as h, t_{ITO} and t_{Spiro}, respectively. 28

Acronyms

a-Si:H hydrogenated amorphous silicon *(p. 3)*
API Application Programming Interface *(p. 11)*
ARC anti-reflection coating *(pp. 3–5, 13, 27)*

BIPV building integrated photovoltaics *(pp. vii, 1, 3, 19, 29)*

CIE International Commission on Illumination *(pp. xii, 8, 23, 29, 31, 53, 54)*
CIGS copper indium gallium selenide *(p. 5)*

DFT discrete Fourier transform *(p. 8)*

FDTD finite difference time domain *(pp. x, xii, xiii, 6, 8, 11, 38–40, 42, 43, 49–52)*
FoM figure of method *(pp. xi, xii, xiv, 6, 9–11, 13, 17–33, 44–48)*

LT light trapping *(pp. vii, xi–xiii, 2, 3, 5, 6, 8, 12, 13, 15–21, 23–27, 29, 30, 32, 33, 38, 40–42, 45–48)*

NIR near-infrared *(pp. 2, 4, 24, 26, 45, 48)*

PML perfectly matched layers *(pp. 38–42)*
PSC Perovskite solar cells *(pp. 1–4, 8, 19, 32)*
PSO particle swarm algorithm *(pp. xii, 9, 10, 13, 17, 18, 20–23, 25, 26, 29, 32, 33, 44–48)*
PV photovoltaic *(p. 1)*

RGB red, green and blue *(pp. xi, xii, xiv, 8, 10, 11, 15, 17–19, 21–23, 25, 27, 28, 32, 44–48)*

TCO transparent conductive oxide *(pp. 3, 4)*

UV ultraviolet *(pp. 2, 3)*

VIS visible *(p. 2)*

Symbols

Abs Simulated absorption per unit volume *(p. 8)*

c Speed of light in vacuum *(p. 8)*
c_1 Cognitive coefficient of PSO particles *(p. 9)*
c_2 Social coefficient of PSO particles *(p. 9)*

e Electron charge *(p. 8)*
$E_{\mathbf{g}}$ bandgap energy *(pp. 1–3)*

$f_{\mathbf{SIM}}$ Central frequency point of the source *(p. 42)*

$g_{\mathbf{Best}}$ Position that corresponds to best value attained for all particles *(p. 9)*

h Planck's constant *(p. 8)*

$J_{\mathbf{SC}}$ Short circuit current density *(pp. v–vii, xi, xii, xiv, 3, 10–13, 15, 17–19, 21–33, 38, 44–48)*

k Extinction coefficient of refractive index *(pp. 3, 7)*

n Real part of refractive index *(pp. 3, 4, 7)*

ω Angular frequency *(p. 8)*

$P_{\mathbf{Abs}}$ Simulated absorption power *(p. 8)*
$p^i_{\mathbf{Best}}$ Position that corresponds to the best FoM obtained by particle i *(p. 9)*
μ Material permeability *(pp. 50, 51)*
ε Material permittivity *(pp. 8, 50, 51)*
ϕ Injection angle of light, in relation to the xy plane *(p. 40)*

θ Injection angle of light, in relation to the z axis *(pp. xii, 29–31, 40, 41)*
$\theta_{\mathbf{SIM}}$ Nominal injection angle of light, in relation to the z axis *(p. 42)*

$\vec{B}$ Magnetic flux density field *(p. 50)*
$\vec{D}$ Electric flux density field *(p. 50)*
$\vec{E}$ Electric field *(pp. 50–52)*
$\vec{H}$ Magnetic field *(pp. 50–52)*
V^i PSO particle-i velocity *(p. 9)*

w Inertia weight constant of PSO particles *(p. 9)*

X^i PSO particle-i position *(p. 9)*

1 Introduction

1.1 Perovskite solar cells (PSCs)

Silicon-based technologies dominate the current global photovoltaic (PV) market, due to their high efficiencies and well-established long-term stability. Nevertheless, the ever-demanding search for increasingly more efficient solar sources has prompted research of other semiconductor materials. Perovskite solar cells (PSC) are one of the most promising new technologies, which have reported an incredibly rapid growth in efficiency, from only 9.7% in 2009 to 25.7% in 2023, making it one of the most efficient types of thin film cells [7]. Despite the significant setbacks regarding the commercialization of this technology — due to stability issues, difficulty in upscaling its production and negative environmental impacts of its lead content — the possibility of bandgap tuning, transparency control and low-energy processing make perovskite solar cells an interesting choice for coloured cells. Moreover, their low thickness is a desirable feature for BIPV, since these devices need to be light-weight for easier application. This material can be manufactured in a variety of surfaces, including flexible substrates, for a relatively low cost [8].

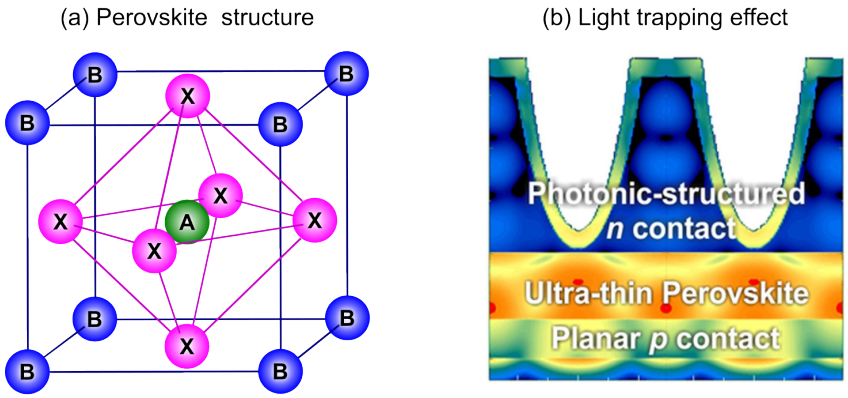


Figure 1.1: (a) Unit cell for the basic ABX_3 halide perovskite structure. Each colour represents different ions: A is the monovalent organic or inorganic cation, B is the divalent metal cation and X is the monovalent halogen anion. (b) Light trapping effect on void-shaped ITO and TiO_2 layers: the red markers in the Perovskite layer represent high absorption zones, due to the near-field forward scattering process promoted by the photonic structures (adapted from [9]).

Halide perovskite semiconductors display a crystal lattice with a cubic, tetragonal or orthorhombic structure, depending on their composition [10, 11]. Their general formula is ABX_3, where A is a monovalent organic/inorganic cation, B is a divalent metal cation and X is the monovalent halogen anion (illustrated in Figure 1.1(a)). For solar cell applications, methylammonium lead iodide ($CH_3NH_3PbI_3$ or $MAPbI_3$) is the most common form of perovskite [12], and also the one used in this thesis. This is due to its high optical absorption coefficient (which allows for the solar cell to be thin while maintaining most absorption), long carrier diffusion length and high carrier mobility, among other optoelectronic properties [4, 10, 11]. Additionally, it is possible to tune its bandgap (E_g) by using its halide-mixed form, $MAPb(I_{1-x}Br_x)_3$ ($0 \leq x \leq 1$) [13, 14]. By substituting I^-

ions by Br^-, there is a distortion of the lattice spacing, due to the different radii of the particles, which results in different values of E_g. As the halide ratio variable, x, increases, the lattice spacing reduces, E_g increases and, consequently, the absorption band decreases in wavelength. This variation results in different colours, from dark brown ($x = 0$), to red ($x = 0.7$), to yellow ($x = 1$).

1.2 Light trapping features

The decrease of the semiconductor's thickness in PSCs has negative implications in the optical performance of the device, as longer wavelengths are no longer absorbed [9]. Some near-infrared (NIR) wavelengths exit the device without being absorbed, as their path in the semiconductor is not sufficient for absorption, resulting in a loss in the spectral response in thin film cells. A strategy to compensate the optical loss in PSCs is the implementation of wavelength-sized nanostructures on the material layers of the cell [8], as exemplified in Figure 1.1(b). These structures have a light trapping effect, as they redirect the incident light rays, promoting forward scattering, longer effective optical path length in the absorbing material (increase absorption in the NIR band) and, in some structures, geometrical refractive index matching for anti-reflection (increase absorption in ultraviolet (UV) and visible (VIS)) [9].

The LT features can be applied to PSCs in different configurations, by structuring different layers, the front and/or rear side of the cell. Front structuring of the device results in better electrical behaviour, contrastingly to structuring the absorber layer, as it avoids surface area increase and consequent surface defects and carrier recombination [8]. Moreover, the photocurrent generated in the cell becomes less angle-dependent, compared to the corresponding planar cell configuration [15]. A variety of LT structures have been designed and can be generally categorized as random/quasi-random or periodic [8]. Periodic structures are easily optimized and usually take inspiration in natural occurrences, such as the moth-eye or monarch butterfly wings. Grating lines (1D and 2D) are the most commonly commercially adapted features on optical devices [16, 17], but some more elaborated geometries have been studied, such as nanopillars [17], checkerboard patterns [16, 17], domes [9], cones and pyramidal configurations [17]. Within these examples, the last two structures are particularly interesting, as their shape creates a transitional gradient of refractive index between the external medium and the top layer of the cell, thus enabling anti-reflection and advancing towards the Lambertian scatterer limit [8]. Notwithstanding the optical improvements of these structures, random or quasi-random LT layouts enhance diffraction effects for a larger variety of frequencies and reduce the angle-dependency of the optical performance of the device, but the optimization of disordered features is much more complex.

Regarding periodic photonic-enhancing structures, numerous studies have investigated how different materials act as LTs on the surface of cells, where high refractive index (n) dieletrics have taken a significant interest [8]. In this category, TiO_2 is a promising

choice, due to its high values of n (which promote scattering and block harmful UV from the perovskite layer) and low values of k (low parasitic absorbance in LTs). In spite of these favourable properties, Sanchez-Sobrado et al. have reported a significant increase in absorption and J_{SC} in hydrogenated amorphous silicon (a-Si:H) cells with void-shaped TiO_2 structures, with respect to the corresponding flat cells, but efficiency growth below 15% [18]. This corresponds to the main problem in dielectric LT features, as these materials have low conductivity and deteriorate the electrical properties of the front contact. Nonetheless, the electrical performance of structured cells can be preserved by employing transparent conductive oxide (TCO) LT features, as these materials are conductive, even when structured [8]. When testing indium zinc oxide LT structures, an efficiency increase of 23.1% was obtained [19]. Additionally, TCO LT structures require lower production complexity, as it corresponds to the same material as the anti-reflection coating (ARC), making this configuration a promising alternative to dielectrics.

1.3 Structural colour

The main sources of colour for a material are dyes or pigments – colour comes mostly from electron excitation and relaxation – and structural colour, where light is selectively reflected for certain wavelengths. While the first case is often the most used method, the parasitic absorption can be quite detrimental to the proper behaviour of solar cells. Structural colour bypasses this problem by using structures, tuned to interact with a specific wavelength of light – not affecting other wavelengths (Figure 1.2(a) and 1.2(b)). Beyond that, they can also be made to scatter light to the absorber material, reducing power conversion efficiency loss and increasing resistance to colour fading [8]. A relevant difference in these colours is their possible dependence on the rotation of structures and on the incident angle of the light. Structural colour can be found in nature: morpho butterfly wings have tree-shaped nano-arrays that produce blue hues and peacock feathers are structured to show a variety of iridescent colours, despite their brown pigments.

As previously stated, different solar cell materials and optical layouts have been explored for BIPV applications, wherein $MAPbI_3$ semiconductors have stood out. First and foremost, it is necessary to understand the different methods available to obtain colour in ultrathin devices. In the past years, different light management techniques, based on light interference, scattering and diffraction, have been applied to solar cells, to provide colour with minimal parasitic absorption. Regarding PSCs, some of the most commonly researched approaches can be grouped into various categories. For instance, as mentioned in Section 1.1, by manipulating the perovskite's bandgap, it is possible to obtain different colours, namely brown, red and yellow shades [4]. Despite the simplicity and cost-effectiveness of this method, a relevant restraint is how limited the colour selection is, as well as the reduction of absorption in the visible spectrum as E_g increases for higher Br content semiconductors.

Regarding structural colour customization by ARC adjustment, studies have been made

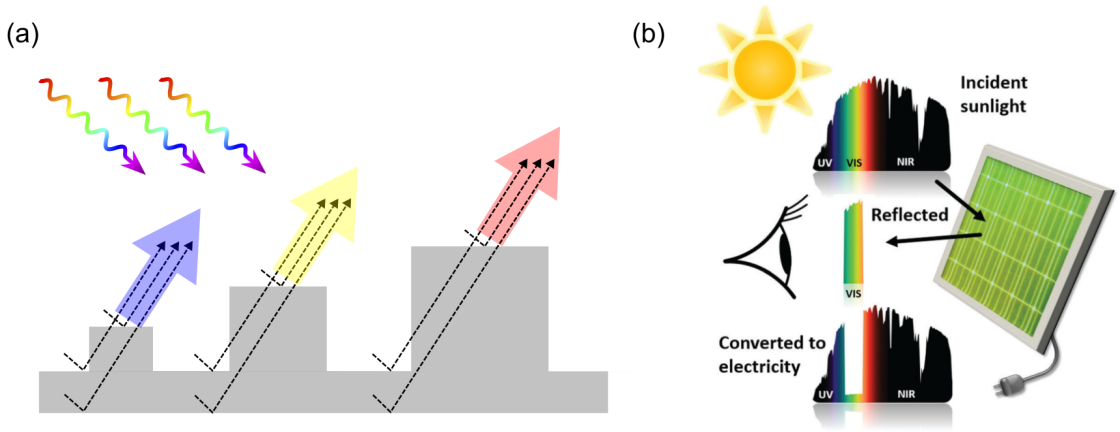


Figure 1.2: (a) Schematic of structural colour generation and respective dependence on geometrical features: different grating sizes result in distinct combinations of light interferences and colours. (b) Illustration of the optical loss associated to colour generation (adapted from [20]).

on PSCs, by testing different TCO thicknesses for different materials, such as PEDOT:PSS and ITO [21, 22]. These concluded that it is possible to obtain a wide variety of colours in the cells, as the selection of height and material (and respective refractive index) of the ARC enables the manipulation of the interference and superposition of light that is reflected and transmitted in each layer [4, 8, 21–23]. Significant losses were observed for NIR frequencies and a relevant drawback in planar colour cells is high colour and photocurrent sensitivity to the angle of light incidence.

The application of plasmonic nanoresonators is an alternative colour structure generation method, as the size and shape of metallic structures, as well as their material, have influence on the reflected wavelength [4, 8]. Lee et al. has demonstrated how the dimensions of metal organized grating nanostrips shift the reflected wavelength [24], and Peharz et al. has reached similar findings, by incorporating Ag nanoparticles on pyramidal surfaces of c-Si solar cells [25]. While these technologies show the capacity of angle-insensitive colour management, throughout the RGB spectrum, simply by controlling the shape and size of plasmonic structures, some obvious downsides include optical losses, due to parasitic absorption at the resonance frequency, and backscattering, which leads to lower external quantum efficiency at visible wavelengths [24, 25].

The implementation of transparent dielectric thin-film coatings, consisting of a sequence of single layers with different refractive indices, can alter the optical properties of devices [26–28]. MacLeod et al. has performed tests on how the different variables of multi-layered dielectric colour filters with two alternating materials (n_1 and n_2) affect the reflection spectra of optical devices. It was concluded that (1) the difference between n_1 and n_2 is a key factor in the determination of the width of the reflection peak, (2) the wavelength of the peak is set mostly by the thicknesses of the layers, (3) the reflection value of the peak strongly depends on the amount of filter layers [26].

Structural colour can also be achieved by including low-loss nano-patterned arrays on the surface of solar cells [8]. This technology promotes forward scattering and longer

effective optical path lengths through the absorber, leading to a general improvement of the quantum efficiency of the solar cell. Additionally, surface structures are also capable of enabling the reflection of narrow peaks in the visible spectrum, while preserving most of the spectral response, which is ideal for a high-performance coloured solar cell. These arrays can be classified as ordered gratings or disordered scatterers, which return angle sensitive colours and angle insensitive colours (matte appearance), respectively.

A theoretical study, carried out by Rao et al., concluded that the addition of organized diffractive gratings to the semiconductor and dielectric medium of a solar cell had positive implications on the current, which is directly affected by the grating parameters: diffraction order, period, height, width and refractive index of the medium [29]. Later, Cho et al. reached similar conclusions regarding the solar cell performance enhancement, owed to organized dielectric gratings, and also introduced their function as colour generators, by regulating the interference of the diffracted waves [30]. A structured ZnO layer was deposited on a copper indium gallium selenide (CIGS) thin-film solar cell, where it was found that the obtained colours and respective brightness were reliant on the previously mentioned grating parameters, as well as the angle and polarization of the incident light.

One of the most popular dielectric materials used to build light trapping features is TiO_2, due to its wide bandgap and environmental stability [8]. The numerical simulation of TiO_2 circular cone-like organized arrays, with stepping layers, on top of an organic solar cell resulted in good colour-filtering properties and a significant decrease of broadband reflection [31]. Therefore, these structures play the role of ARC (due to refractive index matching), light trapping (due to cone-like forms, which redirect the light) and colour filter (stair-like trait, grating period, height and width control the reflection peaks in the visible spectrum). These previous studies [29–31], referring to organized dielectric nanostructures as light trapping and colour filtering features, showed excellent results concerning broadband absorption, which appears to have remained nearly intact, despite the reflection peak associated to colour generation. In fact, the solar cell quantum efficiency increased when integrating the nanophotonic structures for colouring, due to forward-scattering and lower broadband reflection.

The optimization of coloured structurally-enhanced solar cells is a relatively recent development in BIPV, that has shown the most optimistic results relating to aesthetic and electrical performances. On this matter, there is a commercial interest in studying and analysing how different LT structures have the capacity to generate different colours, only by adjusting the cell's layout features. This is explored in this work, by optimizing a selection of coloured photonic-enhanced perovskite solar cells, and understanding how geometry, shape and symmetry affect chromaticity, electric current generation and respective angle-dependency. Additionally, other consumer-oriented products can take advantage of this method to tune structural colour in PV systems, integrated in vehicles, light-powered Internet-of-Things (IoT) and even wearable attires, owing to the versatility of this approach.

2 Simulation methods and setup

The optimization of coloured photonic-enhanced perovskite solar cells was performed by a *Python*™ script, in combination with the *Ansys Lumerical*™ software, via FDTD simulations, by creating a figure of merit and using the particle swarm optimization algorithm. In order to simulate and analyse the optical behaviour of the solar cells, it was first necessary to understand how the 3D electromagnetic simulator, FDTD solutions, modules nanophotonic devices. Annex II and appendix A discuss the underlying solver physics and numerics of this software and what results can be extracted, as well as the specification of simulation conditions, regions, mesh and boundary conditions. The process for the selection of the FoM and further optimization methods are also deconstructed in this section.

2.1 Simulation of photonic devices: *Ansys Lumerical*™ FDTD

This work employs the FDTD method, an approach for solving Maxwell's equations for elaborate systems (based on the Yee algorithm), in which light suffers multiple alterations when subjected to complex structures and non-linear materials [32]. Its time domain nature enables the estimation of a significant range of frequency dependent features in transient simulations, such as transmission and reflection, by exploiting Fourier transforms [33]. This analysis was essential for colour determination, as explained henceforth, in Section 2.2. The FDTD physics solver accounts for the light source's electric and magnetic fields, as well as grid boundaries and non-linear material properties, in order to calculate the field values in various spacial nodes, throughout time, according to the algorithm described in Annex II [33]. Every layout was simulated under similar conditions, except the linear grating lines: due to unmatched x/y symmetry seen in these structures, it was necessary to use two source polarizations (P and S), whereas the remaining structures only required one polarization (P-polarization, as default), as further explained in Annex II.

2.1.1 Simulation layout and setup

This work designed and simulated different photonic-enhancing structures: one-dimensional grating lines, crossed grating lines, domes (prolate semi-spheroids) and circular/squared nanopillars. Figure 2.1(a)-(e) shows the schematics of these structures, while Figure 2.1(g) shows the respective unit cells used in simulations. By studying such a variety of designs, it is possible to understand how the periodicity, shape and size of nano-arrays influence the interference of light and consequent colour generation. Moreover, regarding nanopillars and domes, two different array symmetries, squared and hexagonal, were tested. It has been proven that the photocurrent density can increase substantially when light trapping(LT) structures are set in hexagonal symmetry, which raises interest in testing how the colour is affected [34].

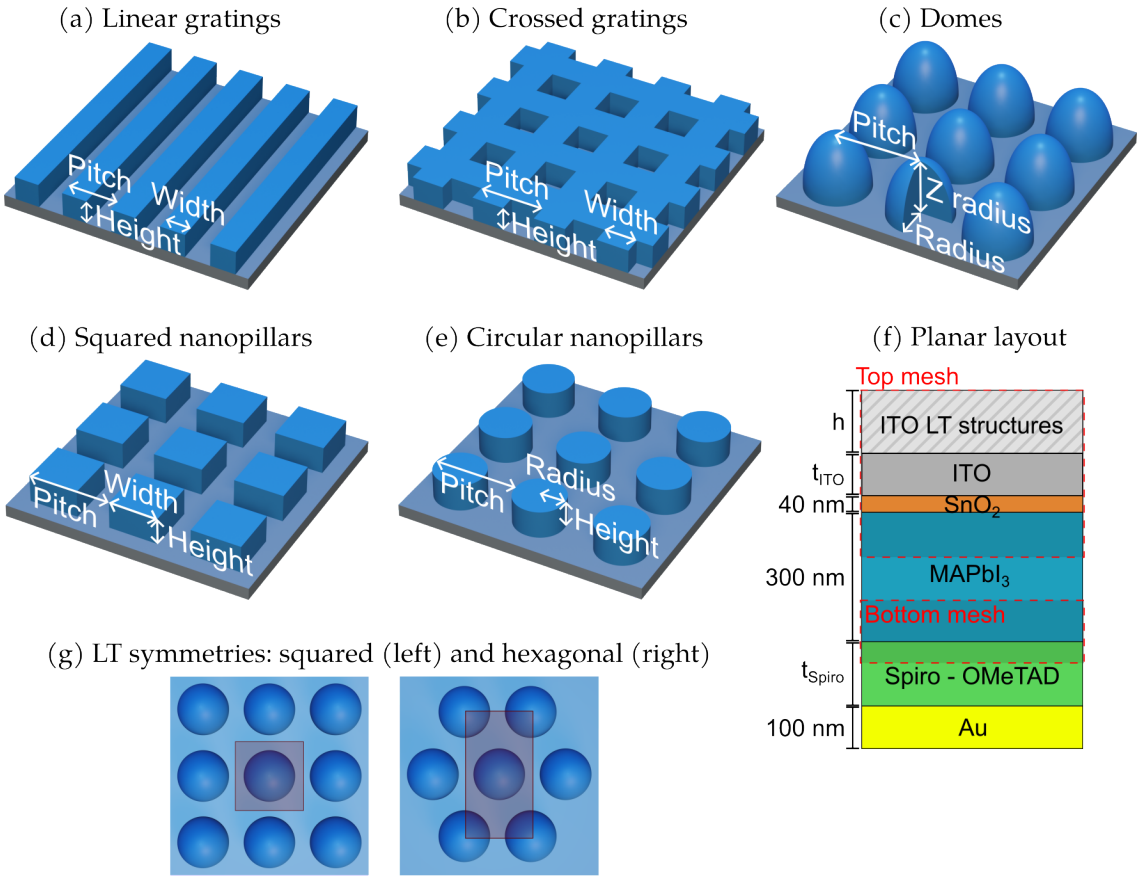


Figure 2.1: (a) - (e) Schematics of the photonic structures analysed in this work, with respective geometrical variables; (f) configuration of planar layers and corresponding thicknesses/height variables; (g) layout and unit cell (red rectangles) for the symmetries tested for circular nanopillars and domes (prolate semi-spheroids): squared and hexagonal. The top layer represents the different structures provided in (a)-(e).

Figure 2.1(f) summarizes the general layer setup used in this thesis. The materials and thicknesses chosen are amongst the most used for each layer to properly establish a connection to experimental work [9]. From bottom to top, the layers are a 100 nm gold metal rear contact, a Spiro-OMeTAD ($C_{81}H_{68}N_4O_8$) hole transporting layer, 300 nm perovskite ($CH_3NH_3PbI_3$) absorbing layer, a 40 nm SnO_2 electron transport layer and an ITO (indium tin oxide) front electrode layer.

The ITO layer was structured with photonic-enhancing light trapping features, where different geometries were tested and the corresponding parameters were optimized. The remaining layers are planar, which facilitates the manipulation of the constructive light interferences and, consequently, the colour output, by optimizing the layers' thickness. Therefore, the optimized geometrical parameters were the thicknesses of the planar ITO and Spiro-OMeTAD layers, and the height, width/radius and pitch of the light trapping structures of ITO.

The materials were modeled in the solver, by inserting refractive index data, both real and imaginary values (n, k), as a function of wavelength, thus being capable of defining

dispersive materials. The tabulated and modeled refractive index plots of the materials used in this work are in Annex I. The photocurrent density generated in the perovskite layer was processed by a solar generation analysis group, that processed Equation (2.1).

$$J_{PH} = e \int \frac{\lambda}{hc} \mathrm{Abs}(\lambda)\, I_{AM1.5}(\lambda)\, d\lambda \tag{2.1}$$

Where Abs is the absorption determined via $\int P_{\mathrm{Abs}}\, dV$, and $P_{\mathrm{Abs}} = \frac{1}{2}\omega\varepsilon''|E|^2$. ω is the angular frequency, ε'' is the imaginary part of the dielectric permittivity, $|E|^2$ is the electric field intensity, V is the absorber's volume, e is the electron charge, h is the Planck's constant, c is the speed of light in vacuum and $I_{AM1.5}$ is the solar power spectrum AM1.5G. This quantity is equivalent to the short circuit current density, since the simulation considers an internal quantum efficiency equal to 1, where the electrical losses are neglected.

The properties of the FDTD simulation region, regarding boundary conditions, monitors and mesh settings, are further explained in Appendix A.

2.2 Colour and optical optimization

The colour of the solar cells was obtained by a *Python*™ script that converts the reflection spectra of the cell, from the discrete Fourier transform (DFT) monitor, to RGB coordinates [35]. This transformation was based on the CIE colour matching functions, explained in Annex III. In essence, the algorithm is capable of reading a power spectrum and determining the corresponding chromatic response (chromaticity), in RGB values, resembling the human eye sensitivity. However, by choosing to simplify the algorithm by ignoring the luminosity, it is possible that, in practice, the cell might not result in the exact same colour as predicted in simulation.

Considering that the ultimate purpose of this study is to develop coloured PSCs with LT structures in different configurations, it was necessary to run an optimization capable of transforming the initial cell layout into a structure with the potential of reflecting light in a certain frequency array in the visible range. This optimization involved creating a new figure of merit, as further explained in Sections 2.2.2 and 3.3.1.

2.2.1 Particle swarm optimization

The cells' geometrical parameters were optimized by adopting a particle swarm method. This algorithm optimizes a system by iteratively improving candidate solutions (particles) with the intent to maximize/minimize a figure of merit, by moving the particle around in the search space (space defined by the variables). This process defines two parameters: the particle position in the search space, and particle velocity (speed and direction of the search) [36]. The evolution of these variables follows a series of steps (further represented in the flowchart in Figure 2.2) [37]:

1. At each time iteration, each particle i computes the value of the fitness function (FoM) at its current position. The particle position is represented as $X^i(t)$, and its velocity as $V^i(t)$. The total amount of particles was set to 25, for 50 iterations.

2. The FoM is obtained for each particle and compared to its previous best value. If the current position of each particle, p^i_{Best}, corresponds to a greater FoM than the best value attained for all particles up to this point, g_{Best}, then the best position of particle i is updated to its current p^i_{Best}.

3. The velocity of the particles is updated, to account for the changes in the last step, in accordance with Equation (2.2). r_1 and r_2 are random numbers between 0 and 1, parameter w is the inertia weight constant (determines the weight that the previous velocity has on the updated velocity, varied from the initial value from 0.9 to the final value 0.4), c_1 and c_2 are the cognitive and the social coefficients (both set to 1.45, determine how much weight should be given between improving the search result of the particle itself - increasing c_1 will lead to further search near the current position - and recognizing the search result of the swarm - when increasing c_2, the velocity favors the best swarm position), p^i_{Best} is the position that gives the best FoM value ever obtained by particle i and g_{Best} is the position for the best FoM explored by all the particles in the swarm.[1]

$$V^i(t+1) = wV^i(t) + c_1 r_1(p^i_{\text{Best}} - X^i(t)) + c_2 r_2(g_{\text{Best}} - X^i(t)) \tag{2.2}$$

4. The particles positions are updated to their improved states, as Equation (2.3) states, which will then guide the movements of the swarm.

$$X^i(t+1) = X^i(t) + V^i(t+1) \tag{2.3}$$

5. If the process has not reached its fixed amount of iterations, the cycle is repeated.

Since the PSO is a stochastic and meta-heuristic solution, it is very likely that, when searching a complex space, defined by many variables, the optimal values correspond to a local maximum, instead of the global maximum of the FoM. To avoid this occurrence, each optimization was repeated multiple times for broad variable ranges, followed by the optimization of a smaller range of variables, according to the best previous results.

2.2.2 Figure of merit

A Figure of Merit is a quantity used to characterize the performance of a system or, in this case, it is a single scalar number selected as the quantity to maximize. To create a FoM for colour application, it was necessary to account for the two factors that must be maximized: the reflection in a particular wavelength range and the photocurrent density of the cell.

[1] The previous PSO settings were based on [38].

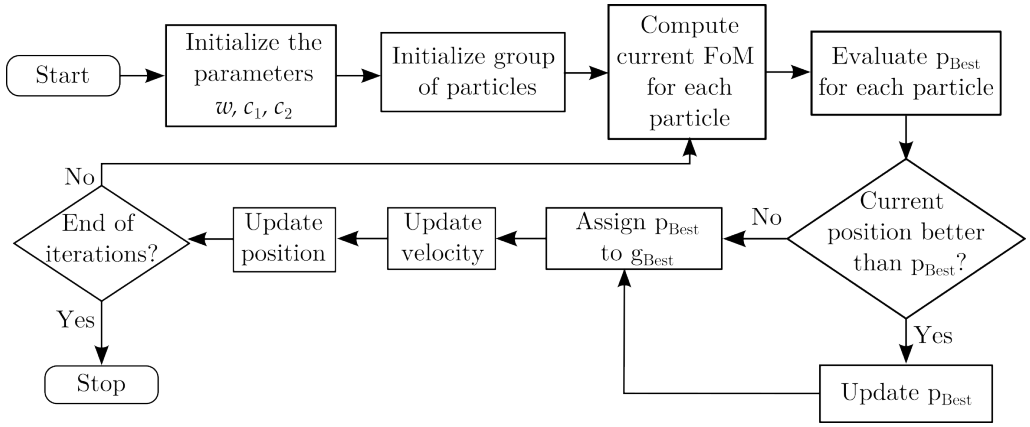


Figure 2.2: Particle Swarm Optimization flowchart – progression of the position and velocity of each particle.

The first step to define the FoM was to select its variables: the current density, J_{SC}, as it is one of the main merit quantities of solar cells, and the euclidean distance (Equation (2.4)) between the RGB coordinates of the required colour (R, G, B) and the colour corresponding to the simulated reflection spectra, at a certain PSO iteration (r, g, b).

$$\text{RGB Distance} = \sqrt{(R-r)^2 + (G-g)^2 + (B-b)^2} \tag{2.4}$$

These variables have been implemented in a previous work [38], in the form of Equation (2.5), which resulted in coherent results. However, it was found that this expression registered some inconsistencies when applied to the optimization algorithm. At times, higher FoM_0 were obtained for low J_{SC} values, since the cell colour corresponded exactly to the requested colour (RGB distance = 0). However, some results registered higher J_{SC} and a very similar colour to what had been demanded (RGB distance barely perceptible to human eyes), but lower FoM_0. This revealed how excessive the influence of the colour of the cell was in the expression, since the eye is not overly sensitive to the colour distance, when defined as in Equation (2.4).

$$\text{FoM}_0 = \begin{cases} J_{sc} & \text{RGB distance} = 0 \\ \dfrac{J_{sc}}{\sqrt{\text{RGB distance}}} & \text{RGB distance} > 0 \end{cases} \tag{2.5}$$

In order to overcome the issues found in FoM_0, a new parameter was conceptualized ("colour limit"), to account for a series of possible cell colours that are almost identical to the stipulated chromaticity, thus attenuating the rigorousness of this feature in the figure of merit. To this end, the colour limit establishes a dividing point in the FoM, where:

- If the RGB distance of the cell is lower than the fixed colour limit, the FoM corresponds to J_{SC}. In this case, the colour of the cell is not relevant to the figure of merit since it has been established (by the initial condition) that the RGB distance is sufficiently low for the human eye to disregard.

- If the RGB distance of the cell is higher than the fixed colour limit, the FoM takes the RGB and J_{SC} of the cell into account. For this condition, different variants of FoM_0 were tested (Equations (2.6) to (2.8) — the analysis and selection of the figure of merit is further explained in Section 3.3.1), where the RGB distance variable was divided by the colour limit, to guarantee continuity in the equation branches of the function. The final version of this expression is defined by Equation (2.7).

$$FoM_1 = \begin{cases} J_{sc} & \text{RGB distance} \leq \text{Colour limit} \\ J_{sc} \times \dfrac{\text{Colour limit}}{\text{RGB distance}} & \text{RGB distance} > \text{Colour limit} \end{cases} \tag{2.6}$$

$$FoM_2 = \begin{cases} J_{sc} & \text{RGB distance} \leq \text{Colour limit} \\ J_{sc} \times \sqrt{\dfrac{\text{Colour limit}}{\text{RGB distance}}} & \text{RGB distance} > \text{Colour limit} \end{cases} \tag{2.7}$$

$$FoM_3 = \begin{cases} J_{sc} & \text{RGB distance} \leq \text{Colour limit} \\ J_{sc} \times \sqrt[3]{\dfrac{\text{Colour limit}}{\text{RGB distance}}} & \text{RGB distance} > \text{Colour limit} \end{cases} \tag{2.8}$$

In summary, the colour system defined in Annex III was integrated in a script, for which an Application Programming Interface (API) connection was made with the *Lumerical*™ software [39]. The FDTD solver read the optimization variables, by adopting a particle swarm algorithm, and the respective reflection spectra was read by the colour script, which returned the RGB values. The script continued the analysis by calculating the distance between the cell's colour coordinates of the particles and the coordinates of the chromaticity in demand (Equation (2.4)), and returning the FoM value. The merit values were recorded and their maximum corresponds to the optimized cell state, for a specific set of geometrical parameters. This process is represented in the scheme of Figure 2.3.

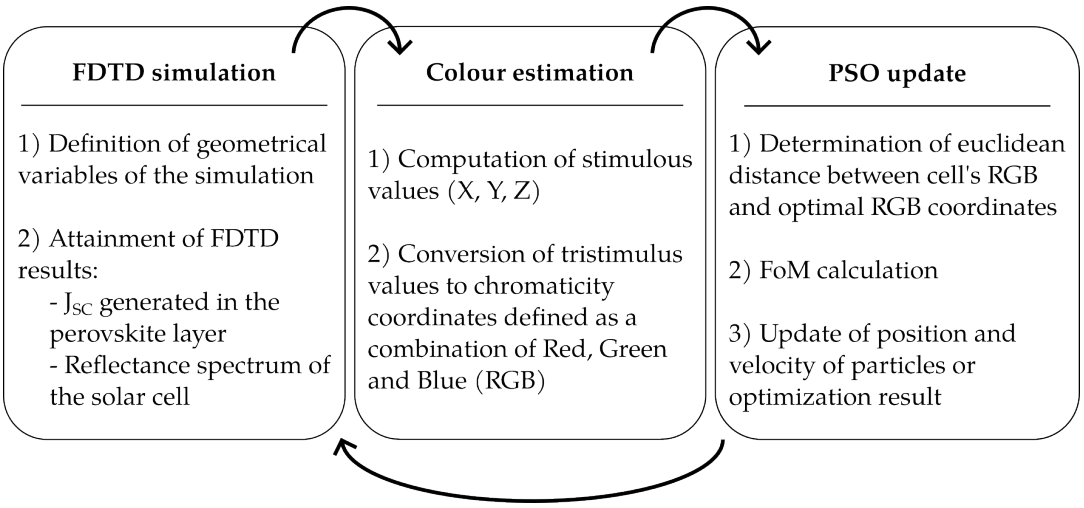


Figure 2.3: Scheme of the method employed in this work and the cycling process that includes FDTD simulations (more thoroughly explained in Section 2.1), reflection/colour conversion (Annex III) and the optimization of the geometrical features of the cells (Section 2.2.1).

3 Results and analysis

This chapter exhibits a variety of analysis regarding chromaticity and optical properties of an assortment of solar cells. Firstly, it was necessary to set out a reference for further studies (Section 3.1), followed by the understanding of the geometrical features and respective influence on merit properties (Section 3.2). This involved numerous variable sweeps, which helped understand the underlying interdependencies between the geometry, shape, symmetry of the cells with light trapping (LT) features and the corresponding colours and J_{SC}. The optimization results are included in Section 3.3, where it is possible to compare the performance of different photonic structures, relating to their capacity to produce certain colours and preserve good optical qualities. It also became interesting to test the optimized cells at oblique angles of light incidence (Section 3.4), as this can affect the previous results.

3.1 Reference cell

The first step of any modeling study is to define an adequate reference cell. Here, this cell will serve as a baseline comparison for the chromaticity (see Section 2.2 and Annex III) and optical performance of the below studied LT-enhanced cells. On that account, by optimizing the flat cell configuration for maximum J_{SC}, it was possible to set an optical standard for the coloured photonic-enhanced cells. By selecting a J_{SC} reference, and further comparing this value to the responses of the enhanced cells, it is possible to validate if the optical loss derived from colour generation does not overpower the optical improvement provided by the LT features.

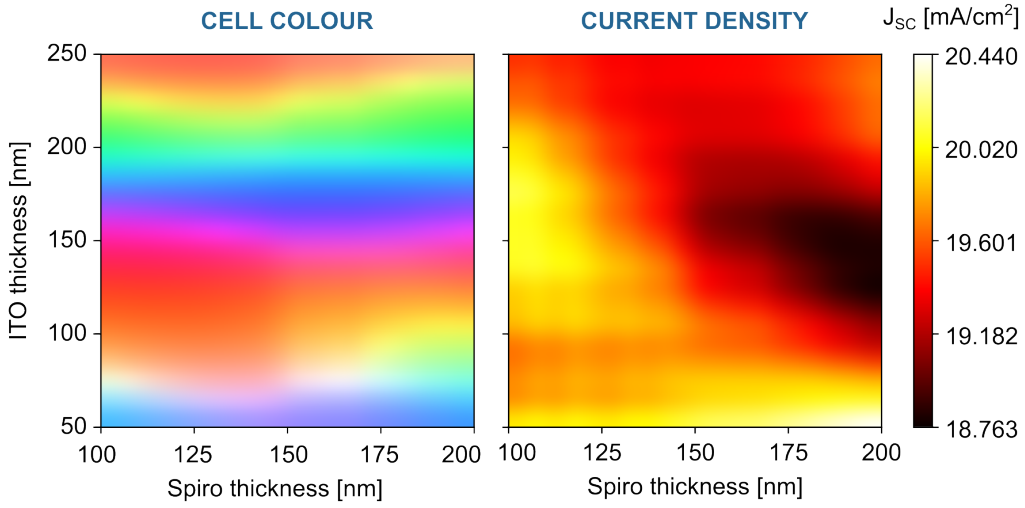


Figure 3.1: Chromaticity and photocurrent density spectra of the planar configuration of the cell, as demonstrated in Figure 2.1 (f), for different combinations of ITO and Spiro-OMeTAD layer thicknesses.

Figure 3.1 shows the determined cell colour (profile on the left) and current density (profile on the right) dependency on the thickness of ITO and Spiro. It is clear that this

configuration can reach a wide range of chromaticities, as most colours of the visible spectrum are present. In these results, the height of the ARC layer has a much more significant effect on the colour of the cell, as it is more superficial, thus having a more pronounced impact on the constructive interference of the reflected light rays. Despite this relation, Figure 3.1 reveals that the generated current is strongly correlated to both thickness values. The optimization of the flat cell, for maximum J_{SC}, resulted in FoM = 206.98 A/m^2, J_{SC} = 20.70 mA/cm^2, for a layout with 168.58 nm ITO and 108.33 nm Spiro-OMeTAD layers.

The results of the multiple PSOs performed for this configuration can be seen in Appendix B.

3.2 Photonic structures

Following the study of the planar configuration of the cell, the analysis of the photonic structures' geometry, shape and symmetry ensued. To this end, the cells were simulated with the structures defined in Figure 2.1, namely linear and crossed gratings, squared and circular nanopillars and domes. Different LT layout symmetries were tested on the latter two structures, squared and hexagonal, to explore if their distribution can result in distinct spectra of colours and current density.

3.2.1 Screening photonic shape and array symmetry

Regarding the study of the shapes of the circular and squared nanopillars, both were tested in a squared symmetry layout (Figure 3.2, left-side schematics), but under a different geometrical condition. The resulting cell chromaticity for a variety of geometrical parameter combinations can be seen, for both configurations, in Figure 3.2. It is clear that the shape does not cause many alterations in chromaticity, as seen from the mostly similar profiles for the circular nanopillars and squared nanopillars in Figure 3.2. Considering this similar behaviour, it was thus chosen to focus on the study of the circular pillars, substantially improving analysis efficiency without significantly losing information. Furthermore, the radial symmetry is also less likely to result in numerical errors, hence increasing the simulation accuracy.

Another relevant aspect to study is the symmetry. Figure 3.3 depicts the chromaticity and current density spectra for circular nanopillars and domes, distributed in squared and hexagonal layouts. Firstly, the current density profiles show higher optical absorption, as supported by previous studies [16]. Concerning chromaticity, the hexagonal symmetry seems to have a larger colour diversity. While the square arrays seem to be mostly localized in blue/pink colours (Figures 3.3 (b) and (d)), the hexagonal arrays (Figures 3.3 (a) and (c)) do seem to extend to orange, red and green. Notwithstanding the higher performance of the hexagonal symmetry, and considering the duration of the simulation of the corresponding unit cell, the difference in the results was deemed insufficient to

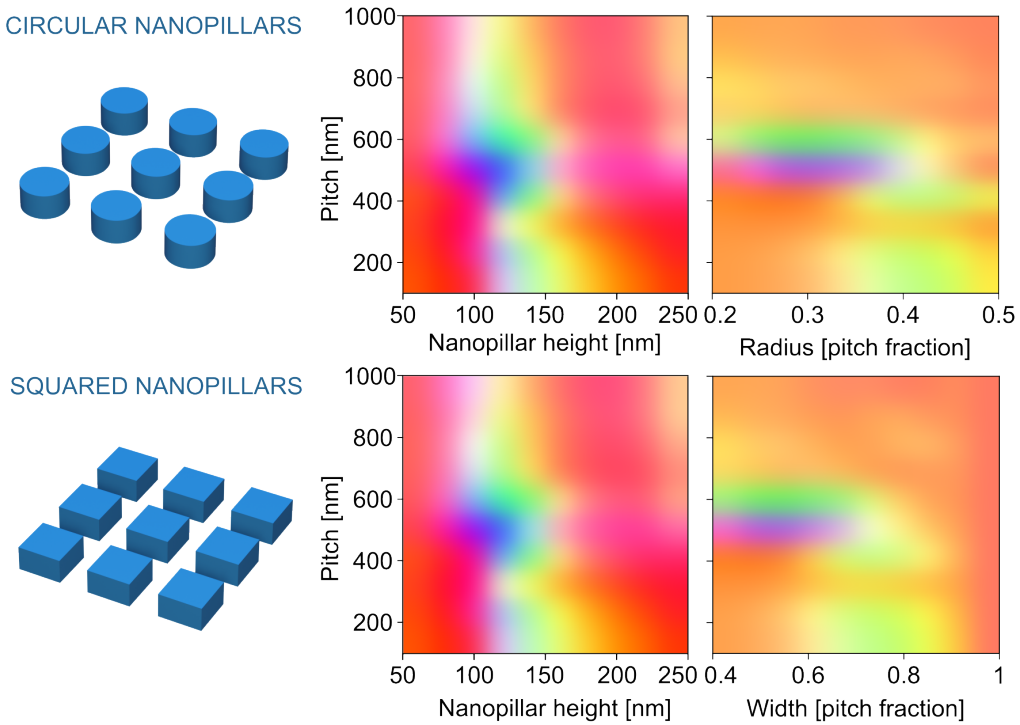


Figure 3.2: Chromaticity for different combinations of structure height and pitch (width fixed at 0.5 and radius at 0.4) and for combinations of pitch and width/radius (pitch set at 500 nm), for circular (top plots) and squared (bottom plots) nanopillars.

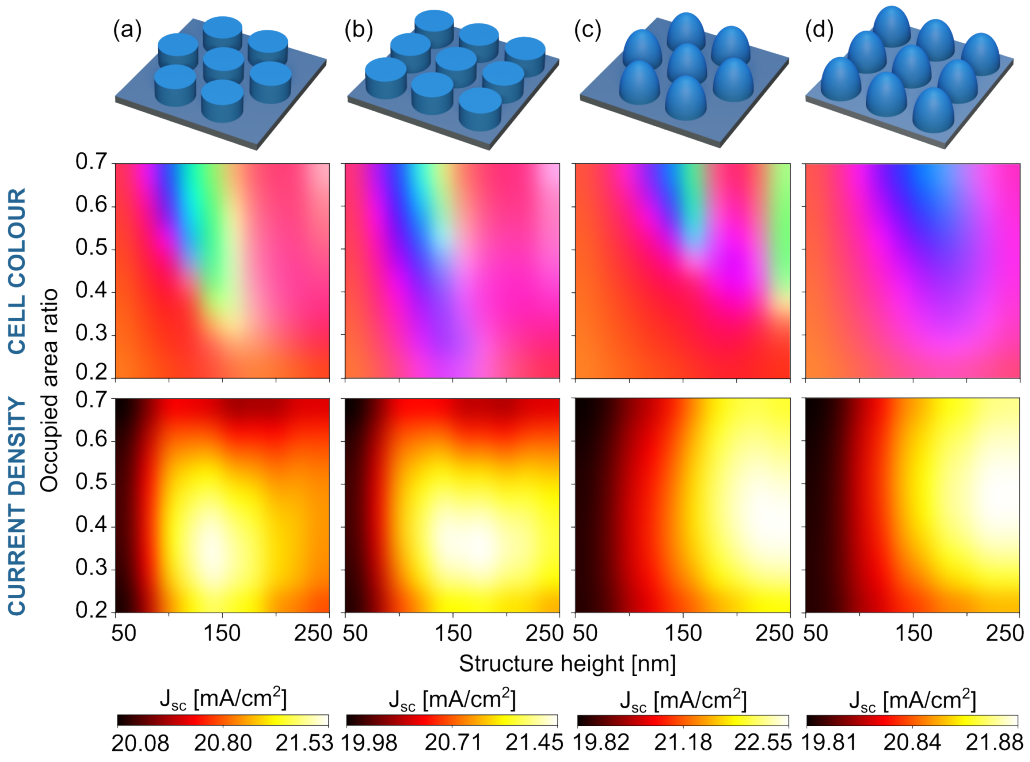


Figure 3.3: Chromaticity and current density for a range of structure heights and volume ratios occupied by the photonic structures, for different layouts of circular nanopillars and domes: (a), (c) hexagonal and (b), (d) squared symmetries. Pitch was fixed at 500 nm for all structures, and planar ITO layer fixed at 50 nm.

justify the optimization of both symmetries, due to time constrictions. As such, the circular nanopillars and domes were optimized in squared symmetry, as this requires lower computational resources.

3.2.2 Analysing photonic geometries

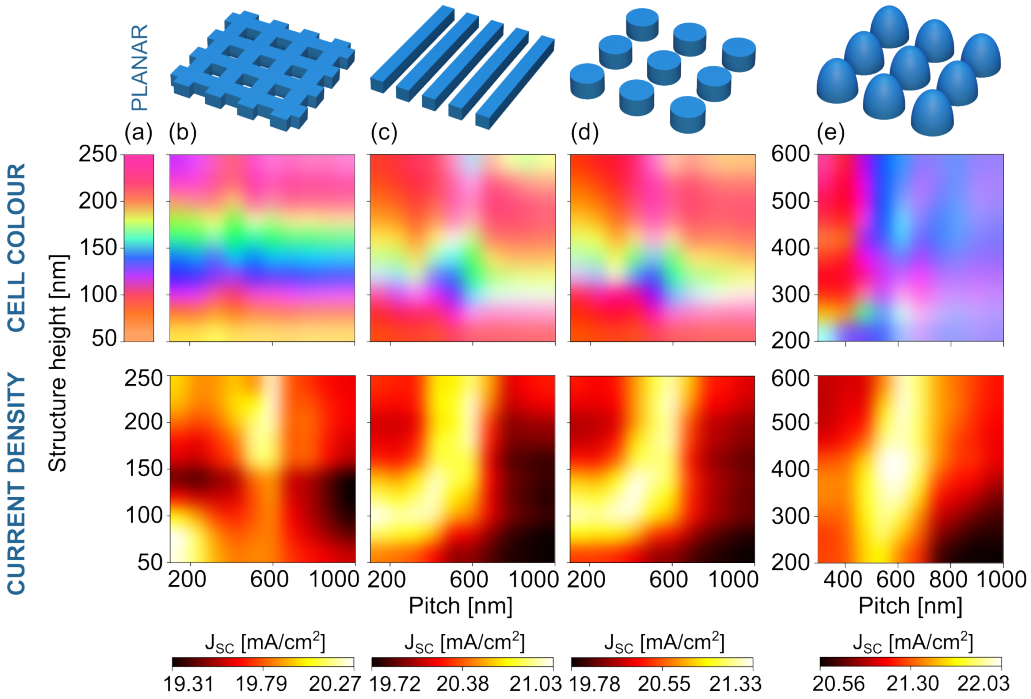


Figure 3.4: Chromaticity (top line of plots) and photocurrent density (bottom line of plots) spectra for different combinations of pitch and grating height (widths fixed at 0.5 and radii at 0.4) for a variety of LT structures: (b) crossed gratings, (c) linear gratings, (d) circular nanopillars, (e) domes (latter two in squared symmetry) and (a) equivalent flat ITO layer.

Figure 3.4 shows the resulting RGB colour spectra dependency on the pitch and height of the different LT structures (colour profiles and top schematics, respectively). The correlation between colour and structure height is particularly strong for crossed gratings, linear gratings and circular nanopillars in squared symmetry. When comparing the colour/height dependency of these structures to the results of a flat cell (where the photonic-enhancing layer was replaced by an ITO planar layer, leftmost profile in Figure 3.4), the colours are identical for the same range of gratings/flat ITO heights. The colour/height dependence is most predominant in crossed gratings, evident by the horizontal bands of chromaticities, and closer to the flat cell chromaticities. Since the cell's colour is defined by the constructive interferences of light, resultant from a series of interface reflections and scattering, it is expected that the height of the crossed gratings exhibit such weight on chromaticity, as it is the most superficial layer. In linear gratings and circular nanopillars, this phenomenon is visible, but less pronounced; moreover, the two former structures show identical RGB and J_{SC} spectra. A possible explanation for these observations is that, as the structures become denser in the unit cell (from pillars to linear

gratings to crossed gratings) the effective refractive index of the structure layer becomes closer to the index of ITO. Consequently, the chromaticity becomes less dependent on the shape or geometry of the photonic structure itself, and more dependent on the above-mentioned interfacial reflections, where the effective index is relevant. On the other hand, the pitch of the pillars and gratings are not as impactful on colour, except for the domes, where the dome height (Z radius) also becomes less relevant in colour diversity. In this particular geometry, its shape creates a refractive index gradient (between air and ITO), which acts as an anti reflection strategy. As such, domes do not follow similar patterns, as the reflection and scattering mechanisms are much more complex.

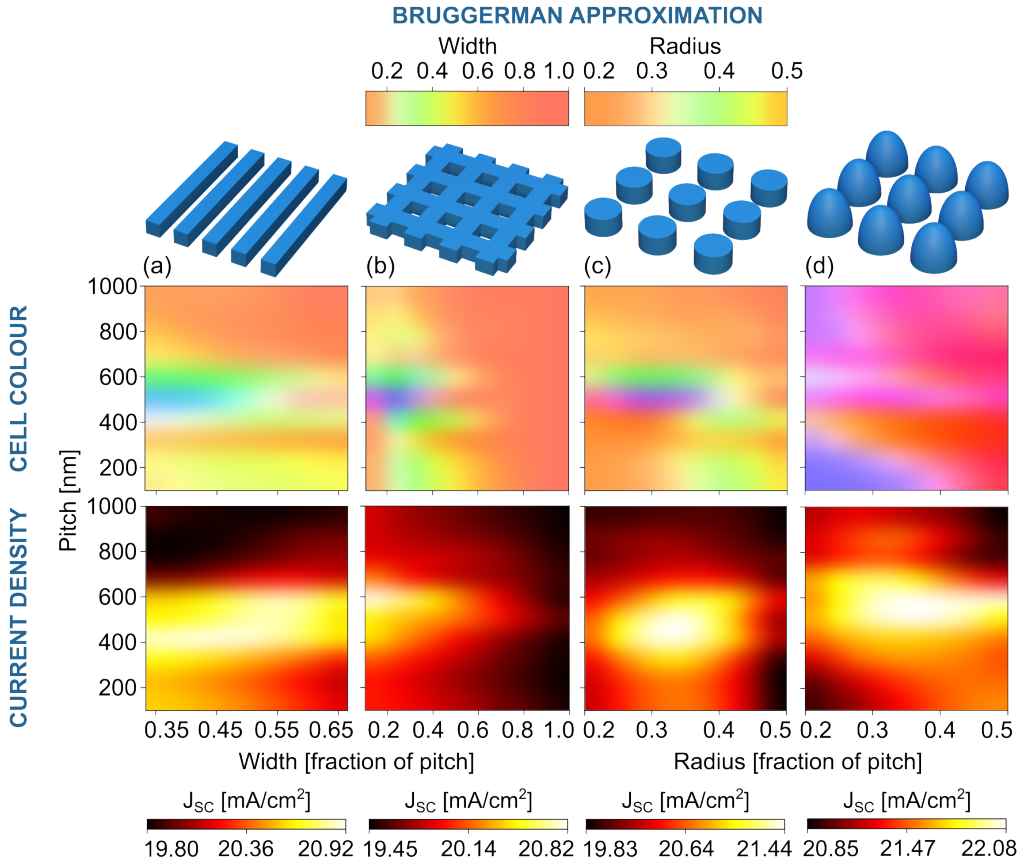


Figure 3.5: Chromaticity (top line of plots) and photocurrent density (bottom line of plots) spectra for different combinations of pitch and width/radius (structure height fixed at 100 nm) for a variety of LT structures: (a) linear gratings, (b) crossed gratings, (c) circular nanopillars and (d) domes (latter two in squared symmetry). The chromaticity of the cells with a photonic enhancing layer equivalent-index planar layer (obtained by the Bruggerman approximation) are also illustrated above, for crossed gratings and circular nanopillars.

Similarly, Figure 3.5 shows the chromaticity and current density, tested for an assortment of pitch and width values. Here, these parameters appear to have minimal effect on the colour spectra, for all structures, as each colour map has the same hues consistently throughout different variable values. To test the previous assumption, regarding the correlation between colour generation and the effective refractive index of the photonic-enhancing layer, the Bruggerman effective medium approximation was applied on crossed

gratings (high unit cell occupation ratio) and on circular nanopillars (low unit cell occupation ratio). These results are provided in the topmost part of Figure 3.5. It is clear that the colours obtained by Bruggerman's method, for a variety of width and radius values, are very similar to those attained by simulation of cells with LT. For lower values of pitch (between 100 nm and 200 nm), the colours observed in LT enhanced cells, for the specified range of width, are identical to the colours derived from the Bruggerman's method, for the equivalent range of refractive indices. However, for higher values of pitch (ergo, bigger LT features), the geometry becomes more relevant for colour selection, as the hues begin to change at pitches higher than 400 nm, even introducing purple chromaticities.

Regarding the J_{SC} spectra, all variables appear to have significant effects on this optical property, registering their highest values for dome-shaped LT features (due to geometrical index matching and forward scattering), and lowest for gratings (linear gratings are simpler LT system and crossed gratings contribute for more parasitic absorption).

3.3 Optimization process

3.3.1 Figure of merit analysis

For any optimization process, it is first necessary to properly define a suitable FoM. This thesis, as detailed in 2.2.2, focused on initially testing Equations (2.5), (2.6), (2.7) and (2.8) on P-polarized grating lines, for magenta (RGB = $(255, 0, 255)$). Here, the search space is defined by different combinations of pitch and gratings height, as presented in Figure 3.6. The core idea here is to see the function behaviour around the FoM maxima. Ideally, the peak should be broad, as to easily guide the PSO particles and avoid highly defined peaks that can be hard to find in larger optimization search spaces. In Figure 3.6, the search space of FoM_0 shows a very low range of FoM values (ranged 58.5 A/m^2), since these variable combinations do not result in the exact RGB coordinate used as input. The highest peaks of the space are very isolated, seen by the small white areas. In the case of FoM_1, the range of FoM has increased substantially (ranged 198.2 A/m^2), since the variable combinations resulted in cells with RGB values within the approved colour limit span (RGB limit was set to 15, as further explained in this section). Moreover, the peaks now seem to be "connected", which facilitates the movement of the particles. However, the regions surrounding the peaks, for FoM_0 and FoM_1, are too flat, which could hinder the movement of the particles and reduce their velocity prematurely. This issue is mitigated in FoM_2 and FoM_3, as seen in Figure 3.6, by the FoM increase in the encircling area of the peaks (zone marked as red is larger). FoM_2 and FoM_3 show very similar results, so the best course of action is to employ FoM_2, since it corresponds to a simpler equation.

To ensure that the new function, FoM_2, performs better than the previously published function, FoM_0 [38], a test was conducted, where both expressions were inserted in the PSO algorithm, and the initial positions and velocities of the particles were equal for both processes. Thereby, it was possible to observe how the particles evolve in the different

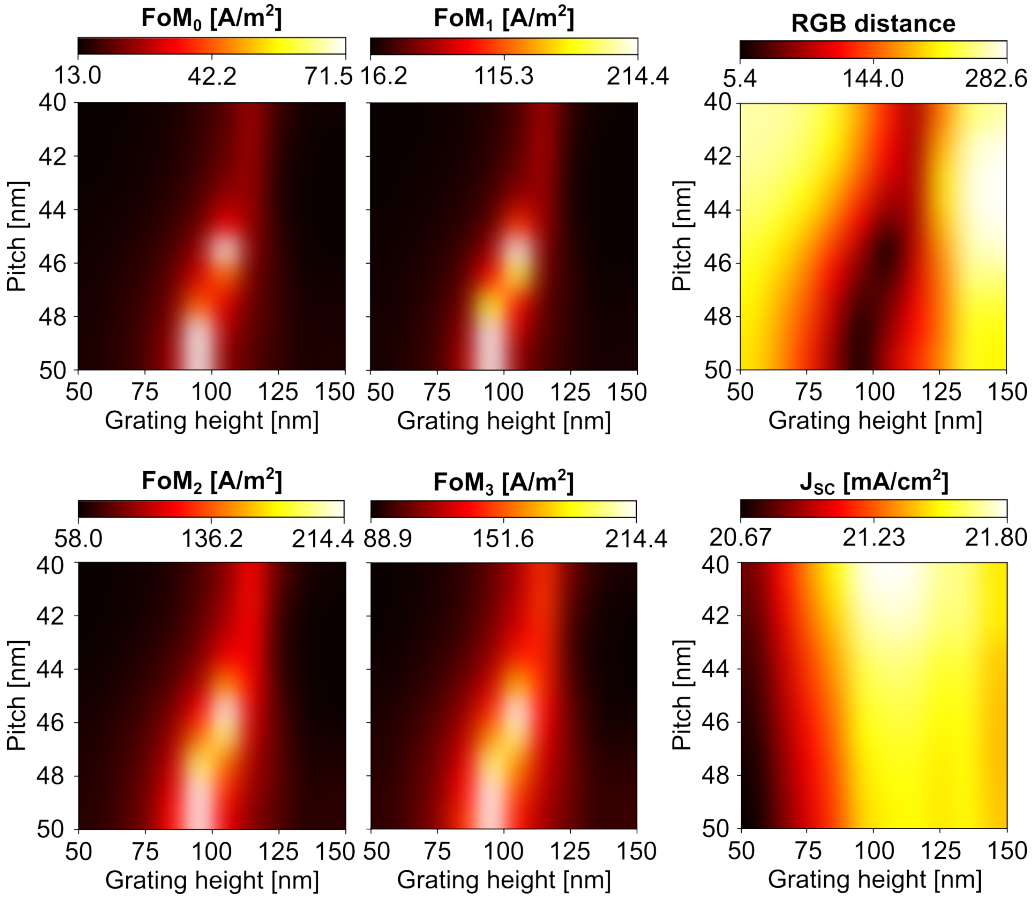


Figure 3.6: Search space defined by Equations (2.5) to (2.8), for different combinations of pitch and gratings height of P-polarized magenta solar cells with linear grating LT features. The variables of the functions, RGB distance and J_{SC}, are also depicted. For FoM_1 to FoM_3, the colour limit was set to 15.

search spaces, without the impact of their initial random distribution. The resulting graphs seen in Figure 3.7(a) show how the values of FoM and J_{SC} evolve, for each particle, for 50 PSO iterations, for the optimization of magenta cells with an RGB limit of 15. It is evident that the optimization that employed FoM_0 converged to lower values of J_{SC} and FoM, while presenting identical chromaticity to the alternative FoM_2 optimization. Since FoM_0 is so strict on obtaining the exact RGB coordinates of magenta, the particles were forced to search for the perfect chromaticity, at the expense of current. On the contrary, in the FoM_2 optimization, the particles were free to search for the maximum J_{SC}, in spaces where the RGB of the cell was sufficiently close to magenta.

At this point, it is possible to affirm that an adequate figure of merit has been created to maximize J_{SC}, in order to provide good electrical and optical properties to the cell, and to approximate the colour of the cell to the specified chromaticity, by minimizing the distances between the corresponding RGB coordinates.

Since the optimization of solar cells with complex geometries are very time-consuming and computationally challenging, it was necessary to carefully select a significant quantity of colours to optimize, so as to provide all the necessary information. To minimize the

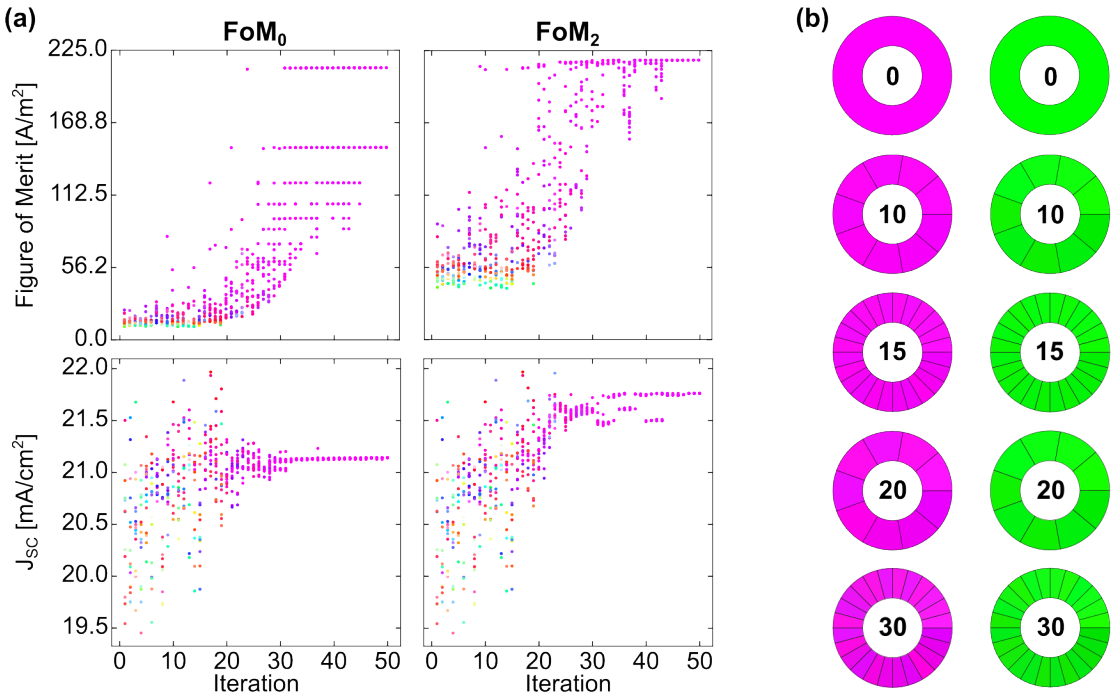


Figure 3.7: (a) Progress of FoM and J_{SC} values for 15 particles in the optimizations (50 iterations) of magenta solar cells with linear grating LTs (P-polarized), for a fixed initial seed, using FoM_0 (left column) and FoM_2 (right column, for a colour limit of 15). Each scatter point represents one particle and the corresponding cell colour. (b) Colours at a series of RGB distance (between 0 and 30, calculated by Equation (2.4)) from magenta, $(255, 0, 255)$, and green, $(0, 255, 0)$.

amount of simulations, two cell colours were implemented: magenta (RGB = (255, 0, 255)) and green (RGB = (0, 255, 0)). These were chosen since they represent all the primary colours of the sRGB spectra, green, red and blue, with the latter two being represented by the colour magenta (the requirement of two reflection peaks simultaneously reveals how the method responds to complex chromaticities).[1] Green is interesting to apply on these cells as well, since this colour was seldom present in the preliminary studies. Additionally, this wavelength band (495 nm–570 nm) usually presents a peak in the absorption spectrum of solar cells, thus heavily contributing to generation of current. As such, these chromaticities were chosen to challenge the method of this work, despite the BIPV market demands.

Figure 3.7(b) depicts the RGB chromaticities at certain RGB euclidean distances from magenta and green, where it is possible to select the maximum distance that is considered acceptable for this study (FoM parameter "colour limit"). For easier comparison, the same value of 15 was chosen for both magenta and green cell simulations.

Based on previous analysis and simulations, including the results in the former Sections 3.1 and 3.2, it was necessary to set limits for the geometrical parameter optimization.

[1] It is important to note that obtaining magenta does not imply that the same cell is capable of producing red and blue. Nevertheless, the colour blue is very commonly seen in commercially available silicon-based photovoltaic panels and red PSCs have been produced before, by tuning the perovskite's bandgap.

Considering that this method is somewhat complex, since the merit figure encompasses two requirements (colour and current density) and optimizes 5 parameters, the variable ranges were considerably large. These can be seen in Table 3.1, for every configuration.

Table 3.1: Variable ranges [bottom limit, top limit] used in the optimization of planar and enhanced solar cells, for magenta and green.

Variables	**Planar**	**Linear gratings**	**Crossed gratings**	**Circular nanopillars**	**Domes**
Pitch (nm)	NA	[100, 1000]	[100, 1000]	[100, 1000]	[250, 1000]
Width/Radius (pitch fraction)	NA	$\left[\frac{1}{3}, \frac{2}{3}\right]$	$\left[\frac{1}{3}, \frac{2}{3}\right]$	[0.2, 0.5]	[0.2, 0.5]
Structure height (nm)	NA	[50, 250]	[50, 250]	[50, 250]	[50, 1000]
ITO thickness (nm)	[50, 250]	[50, 250]	[50, 250]	[50, 250]	[50, 250]
Spiro thickness (nm)	[100, 200]	[100, 200]	[100, 200]	[100, 200]	[100, 200]

In terms of variable restrictions in the optimizations, as mentioned in the previous section, the width or radius of the structure is defined as function of the pitch and, in the case of LT domes, the Z radius was limited by the radius: Radius $\leq$ Z radius $\leq$ 2 $\times$ Radius. This avoids high aspect ratios and future production irregularities. These dependencies and restrictions may cause problems in the PSO algorithm, as particles may have difficulty converging in the viable interval of Z radius; furthermore, the pitch and radius converge simultaneously, which can prevent the optimization of the dependent variable. To guarantee proper variable convergence, several optimizations, followed by zooms in the search region, are performed. This method tries to minimize the stochastic nature of the algorithm (explained in Section 2.2.1). The variable ranges from Table 3.1 were inserted into the PSO script, and run multiple times, resulting in different values, in most events, due to the stochastic nature of the algorithm and the complexity of the search space. If the variables converge around similar values, it is likely that the global maximum of the FoM is near these regions, but the particles' velocities might have reduced in local maxima, before exploring the region completely; hence the necessity to run additional PSOs for zoomed ranges of variables, when under these circumstances.

3.3.2 Optimization results: planar solar cells

The optimization of the flat solar cell only considered two variables: the thicknesses of the ITO and Spiro layers. It is important to obtain the optimal geometries of the planar

layers of the cells, as this also serves as a reference for future optimizations of cells with LT features.

Figures 3.8(a) and 3.8(b) show the variable grid setup that describes the optimization results – in particular the J_{SC}, FoM and RGB distance (for a colour limit of 15) – for magenta and green, respectively. This profile shows both the results using the initial simulation domain, via the circle-shaped points, and the results using a zoomed domain (light blue highlighted region and star-shaped points). This method allows for an efficient and easy way to compare both these results. Moreover, the final optimization results for all the structures are summarized in Table 3.2, along with the respective cell illustrations.

The analysis of the variable grids in Figure 3.8(a) reveal that the wide range optimizations resulted in similar thicknesses of ITO and Spiro (around 150 nm and 100 nm, respectively), but different values of J_{SC}. To verify the possibility of a higher peak, two additional PSOs were performed, for smaller variable ranges: ITO ranged between 125 nm and 200 nm, and Spiro ranged between 100 nm and 125 nm. For this structure, as the zoomed optimizations did not improve the previous results, the best PSO registered FoM = 117.11 A/m^2 and Jsc = 20.69 mA/cm^2.

Analogously, the optimizations of the green flat solar cell resulted in different sets of layer thicknesses, as seen in the grid plots from Figure 3.8(b). In this case, the zoom range of the Spiro thickness was not focused on the region with most amount of results, but around the best FoM (green marker, at 200 nm); this is an example in which the particles of the PSOs marked by red and blue were confined in same local maximum (Spiro thickness 100 nm), whilst the green marked PSO particles were able to find a higher maxima. Accordingly, the zoomed ranges were set to [175, 250] nm and [175, 200] nm, for ITO and Spiro thicknesses, respectively, which resulted in the best FoM of 72.85 A/m^2, with Jsc = 20.04 mA/cm^2 (3.14% loss, relative to the reference).

Following the previous analysis, it was observed that neither the magenta nor green flat cells were capable of generating an RGB within the colour distance limit set in the FoM. Regardless, the magenta flat cell registered higher FoM and J_{SC}, at a lower RGB distance. Additionally, by examining the reflection spectra of both cells, in Figure 3.8(c), it is clear that the magenta flat cell is very close to the reference cell (with identical J_{SC} values), thus exhibiting higher J_{SC} than the green planar cell. In spite of relatively low merit values, these spectra show well-defined reflection peaks around the blue, red and green regions, at reflection values around 20%, and the resulting chromaticities were still recognizable as magenta and green hues.

3.3.3 Optimization results: crossed gratings

The crossed gratings solar cells optimized five variables: the pitch, width and grating height of the structures (as represented in Figure 2.1) and the thicknesses of the planar ITO and Spiro layers. This forms a much more complex search space in the optimization algorithm, compared to flat cells. The results of the multiple PSOs performed for this

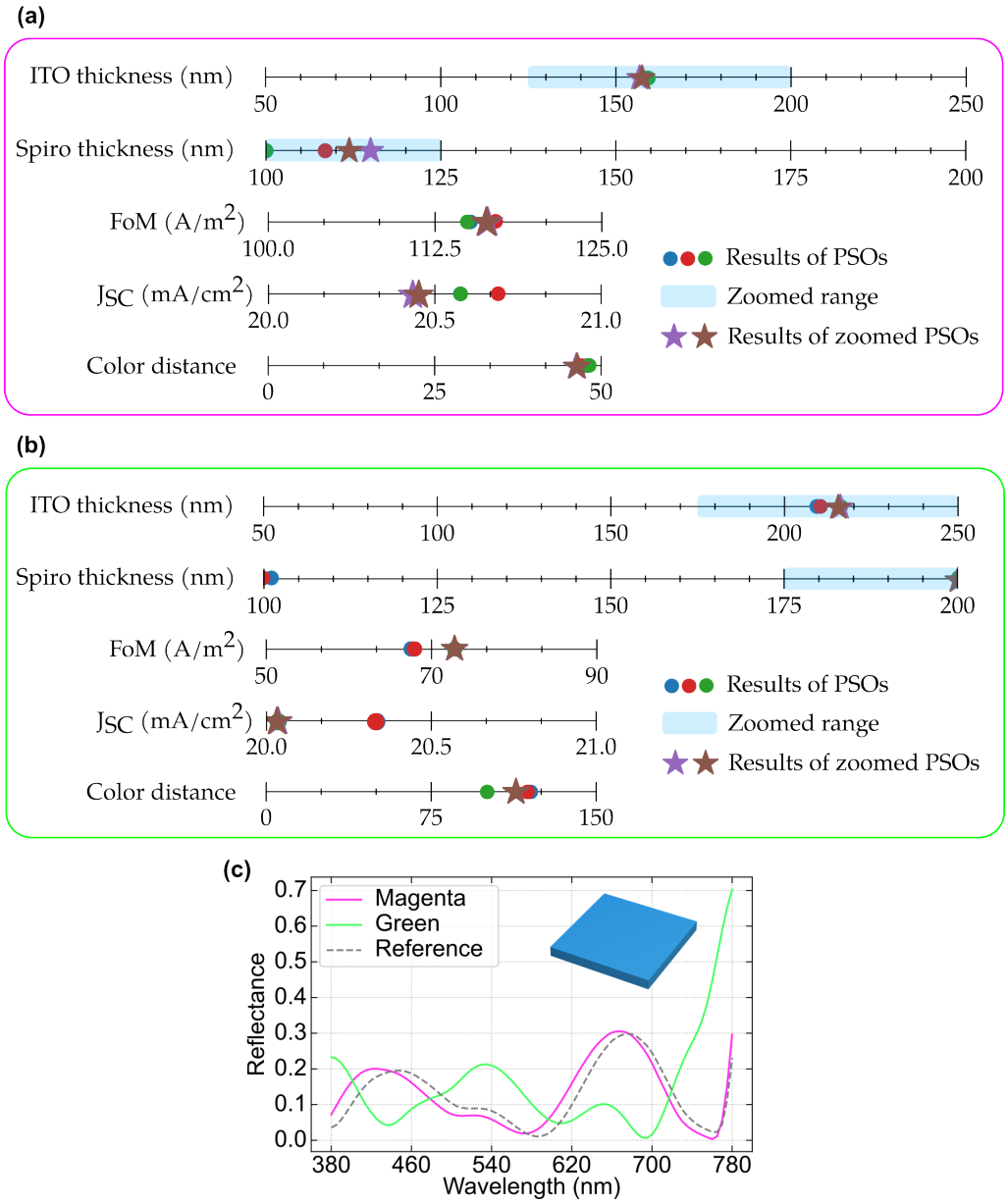


Figure 3.8: Optimization results for the (a) magenta and (b) green flat cells, for the full optimization range and the zoomed optimization range (light blue marked region). Each profile shows the main optimization variables (ITO and Spiro thicknesses) and the resulting FoM, J_{SC} and Colour Distance for each optimization; the circle-shaped points mark the full-ranged optimization results and the star-shaped points the zoomed optimization results. (c) Reflection spectra of the optimized flat cells for magenta (magenta line), green (green line) and reference cells (dashed line).

configuration can be seen in Figures 3.9 and 3.10.

As visible in Figure 3.9, most results of the PSOs were able to reach RGB distances lower or equal to the colour limit, set at 15, which resulted in FoM values identical to J_{SC}, as indicated by Equation (2.7). After running the optimizations with zoomed parameter ranges, the best FoM result was 217.60 A/m^2, for J_{SC} = 21.76 mA/cm^2 (5.18% increase relative to reference), and the respective geometry can be seen in Table 3.2.

Despite how easily the algorithm found a geometry able to generate magenta, some

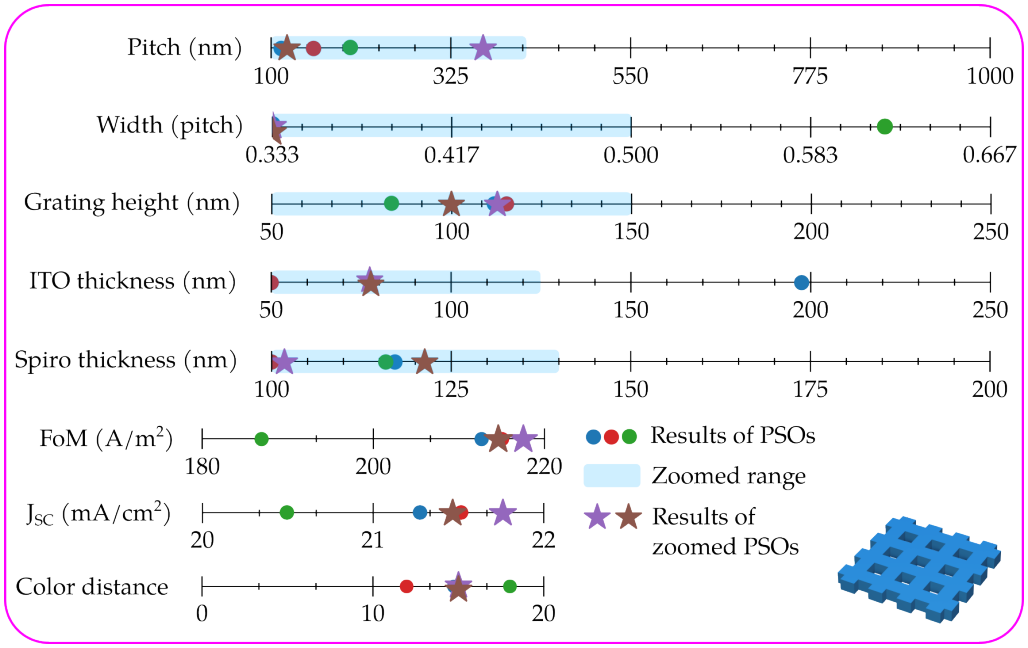


Figure 3.9: Optimization results for magenta solar cells with crossed grating LT features, for the full optimization range and the zoomed optimization range (light blue marked region). Each profile shows the main optimization variables and the resulting FoM, J_{SC} and Colour Distance for each optimization; the circle-shaped points mark the full-ranged optimization results and the star-shaped points mark the zoomed optimization results.

complications arose in the optimization of the green configuration. As represented in Figure 3.10, the four optimizations with wide parameter ranges resulted in relatively low FoM values, due to high RGB distances. After analysing and verifying the correct performance of the PSO particles, throughout the iterations (there were no anomalies or early convergences in the process), it was concluded that this cell configuration was not able to produce a chromaticity within the interval of green RGBs demanded by the colour limit parameter, defined in the FoM. To overcome this matter, and be able to attain higher values of J_{SC}, the colour limit was increased from 15 to 30, to broaden the maxima peaks of the search space. This change is not problematic for this method, since the RGB distances in the green zone of the CIE colour gamut are not as easily perceptible by the human eye, according to the MacAdam ellipses, referred in Annex III. As such, an RGB distance of 30 is not as evident in green cells as in magenta cells, as clearly demonstrated in Figure 3.9. After this alteration, the best PSO was able to obtain FoM = 210.62 A/m^2, J_{SC} = 21.06 mA/cm^2 (1.79% increase relative to reference) at an RGB distance of 29.83 (further results in Table 3.2).

The effect that the structures have on colour generation and reflection peak selection can be extrapolated from the spectra in Figure 3.11 (right plot), where the reflection spectrum of the optimal magenta cell shows that the crossed gratings act as a perfect filter for light in green wavelengths (495 nm - 570 nm), while also increasing the reflection peak in red (620 nm - 750 nm) wavelengths (this is inferred by comparing the spectra of the optimized cell with and without photonic features). By comparing these same spectra, the

contribution of the structures as anti-reflective elements and forward scatters is visible by how the overall reflection of the cell is reduced by their presence. Regarding the green cell (Figure 3.11, left plot), it is clear that the configuration was not able to completely filter the reflection in the red and blue regions, where subtle peaks are still present. Moreover, the reflection in the NIR zone seems to have increased, relative to the reference cell, which might explain why the J_{SC} was lower for this chromaticity. Nevertheless, the optimal geometry of the solar cell shows reduction of broadband reflection.

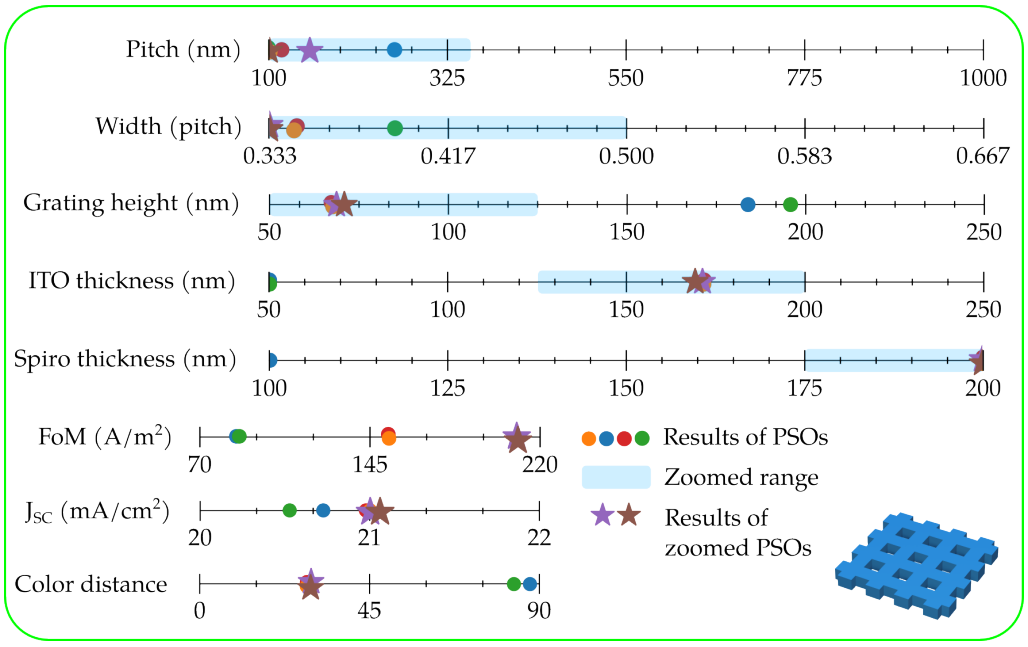


Figure 3.10: Optimization results for green solar cells with crossed grating LT features, for the full optimization range and the zoomed optimization range (light blue marked region). Each profile shows the main optimization variables and the resulting FoM, J_{SC} and Colour Distance for each optimization; the circle-shaped points mark the full-ranged optimization results and the star-shaped points the zoomed optimization results.

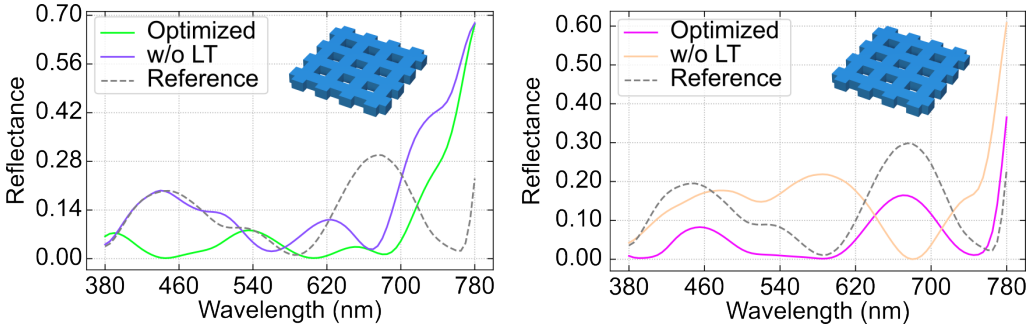


Figure 3.11: Reflection spectra of optimal solar cells with crossed grating, with ("Optimized") and without ("w/o LT") photonic structures, for green (left plot) and magenta (right plot), and respective reference spectrum. The solar cell colours were applied to each corresponding lines.

3.3.4 Optimization results: domes

The solar cells with domes, defined by half spheroids, had five optimization variables: the pitch, radius and Z radius (dome height) of the structures (as represented in Figure 2.1) and the thicknesses of the planar ITO and Spiro layers. As previously mentioned, the parameter Z radius was restricted between the values of the radius and the double of the radius of the domes, for wide ranged PSOs; for the zoomed PSOs, this restriction was lifted, since the Z radius range was small-scaled and could no longer result in drastic aspect ratios. Since this limitation can cause problems in the convergence of this variable, broad zoom ranges were selected.

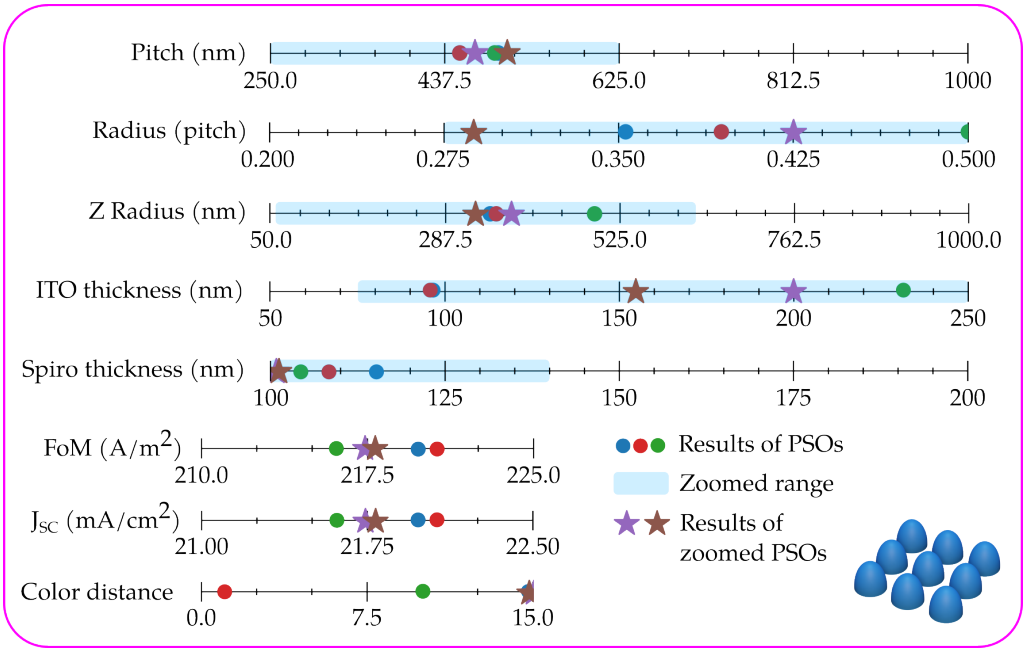


Figure 3.12: Optimization results for magenta solar cells with domes, for the full optimization range and the zoomed optimization range (light blue marked region). Each profile shows the main optimization variables and the resulting FoM, J_{SC} and Colour Distance for each optimization.

Figures 3.12 and 3.13 show the variable grid with optimization results for magenta and green cells with domes, respectively. By analysing Figure 3.12, it is possible to conclude that these LT structured cells located FoM maxima peaks with ease, showing that a variety of geometries could generate colours very similar to magenta, within a color distance of 15. The parameter zoomed optimizations did not improve the results, which showed that the Z radius limits did not affect the process significantly. The best PSO resulted in FoM = 220.66 A/m^2, for a J_{SC} record of 22.07 mA/cm^2 (6.68% gain), in this work. When optimizing green cells with domes, the colour limit was not increased (unlike for cells with linear and crossed gratings), since the PSOs were able to attain values of RGB distance below 15 (Figure 3.13). Similarly to previous configurations, the green cell with domes resulted in lower FoM and J_{SC} than the magenta cell. Nevertheless, this configuration set the merit record for green cells, with FoM = 213.96 A/m^2 and J_{SC} = 21.40 mA/cm^2 (3.44% gain). Further PSO and geometry results are present in Table 3.2.

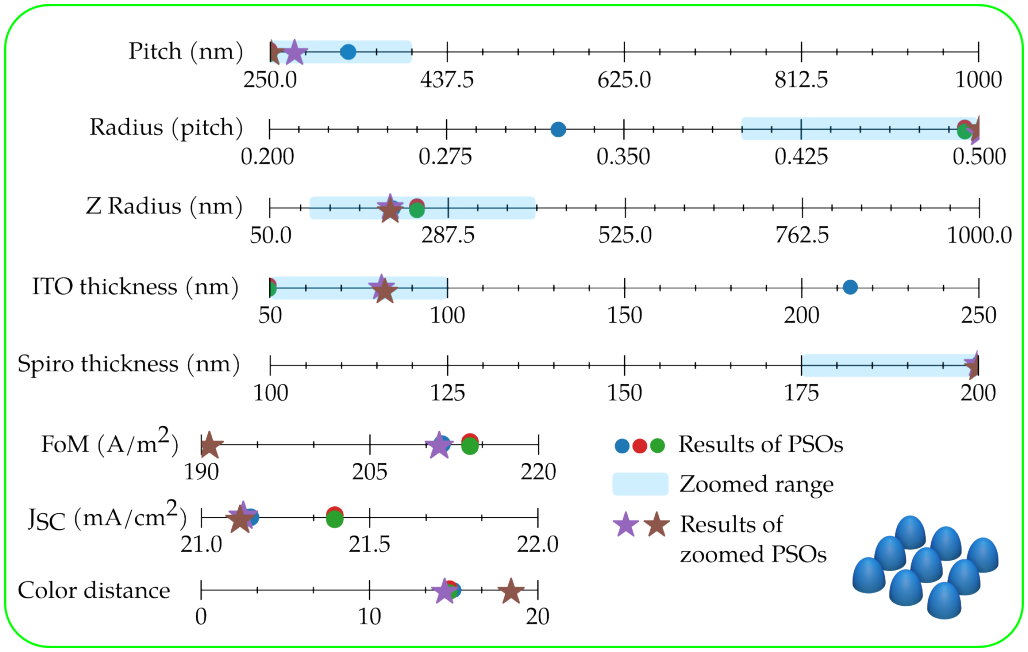


Figure 3.13: Optimization results for green solar cells with domes, for the full optimization range and the zoomed optimization range (light blue marked region). Each profile shows the main optimization variables and the resulting FoM, J_{SC} and Colour Distance for each optimization.

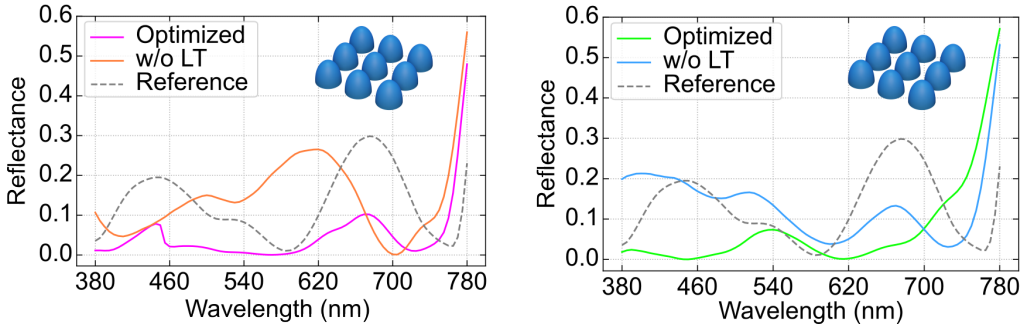


Figure 3.14: Reflection spectra of optimal solar cells with domes, with ("Optimized") and without ("w/o LT") photonic features , for green (left plot) and magenta (right plot), and respective reference spectrum. The solar cell colours were applied to each corresponding lines.

With regard to the reflection spectra of the optimal magenta cell, Figure 3.14 shows that the domes promote significant absorption enhancement and a clear filtration of the wavelengths in the green region (495 nm - 570 nm). For green cells, the domes also suppress the reflection peaks in red (620 nm - 750 nm) and blue (450 nm - 495 nm) wavelength regions, but increases in the NIR region, possibly contributing for the lower value of J_{SC}, compared to the magenta cell.

3.3.5 Optimization results: overlook

After a closer analysis of the optimization of magenta and green cells in flat configuration and with crossed grating and dome LT features, the remaining structures and respective PSO grid plots can be seen in appendix B, as they follow analogous examinations.

At this point of the study, it is possible to compare how the different photonic structures performed, in regard to optical performance and capacity to generate the selected colours, with the FoM, J_{SC}, RGB and geometrical attributes in Table 3.2, and all the above in the plots of Figure 3.15.

First and foremost, the optimizations of flat cells resulted in the lowest merit values, since they (1) were unable to find geometrical configurations that corresponded to the selection of chromaticities demanded by the FoM and (2) did not take advantage of the forward scattering and geometrical index matching anti-reflection provided by LT features. On this thought, this study has already proven how photonic-enhanced solar cells with LT top structures are a superior method to attain structural colour, compared to flat cells' ARC thickness refinement.

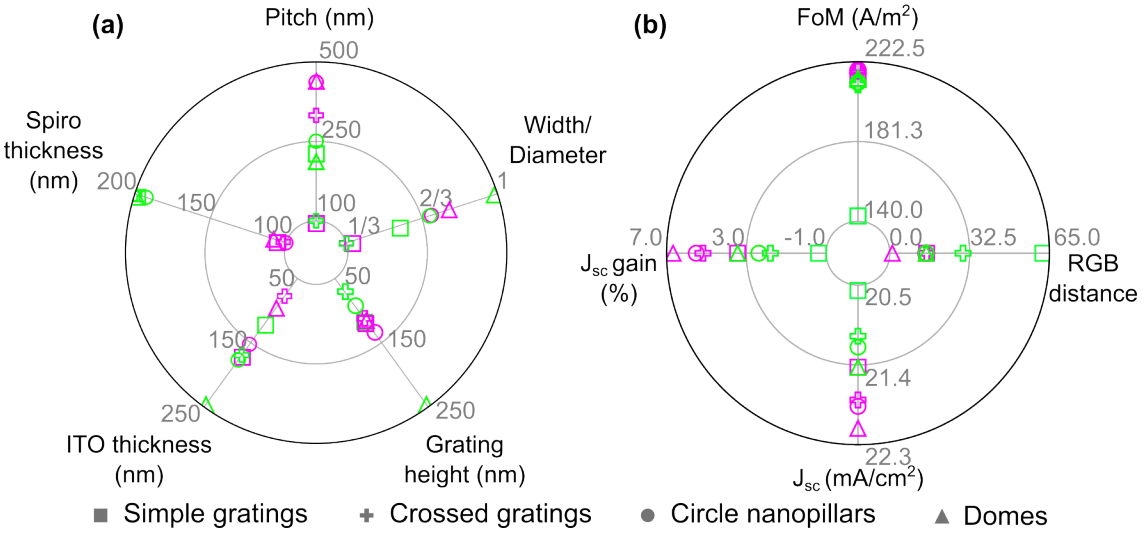
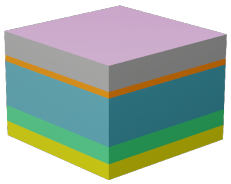
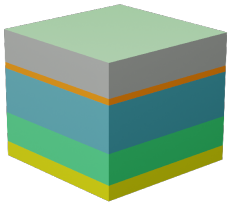
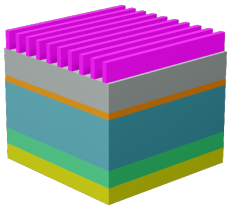
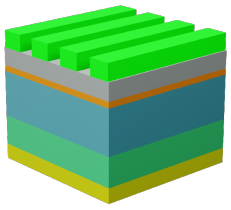
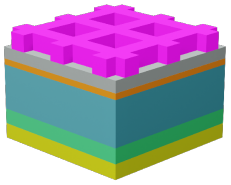
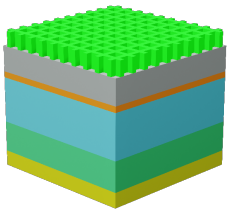
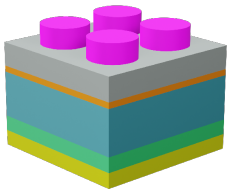
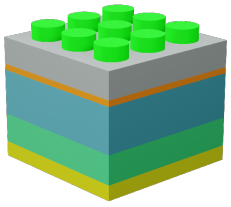
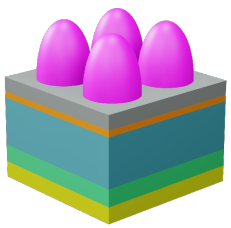
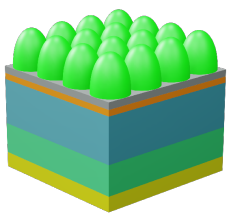


Figure 3.15: (a) Optimal geometry parameters of photonic-enhanced solar cells and (b) corresponding J_{SC}, J_{SC} gain (relative to reference), FoM and RGB distance values. The colours of the markers correspond to the chromaticity of the cell.

In respect to the photonic enhancing featured solar cells, it is clear that, for most cases, the structures converged to larger geometries to generate magenta, compared to green (with the exception of linear gratings), as evident in the size-accurate illustrations in Table 3.2 and by the tendency in Figure 3.15(a) – the photonic feature sizes (pitch, width, height) for the magenta points, indicating the magenta-optimized results, are at higher values than the green points, indicating the green-optimized results. Moreover, a pattern can also be observed regarding the thicknesses of the planar layers (ITO and Spiro), that frequently show higher values for green cells, as seen in Figure 3.15(a). It is also worth noting that the radius and width of half of the structures – crossed gratings and circular nanopillars – converged to identical pitch fraction values for both colours, supporting that this parameter does not have strong influence on the chromaticity, and converges with the intent to maximize the J_{SC} (as predicted in Section 3.2.2).

Overall, despite the complexity of the reflection spectrum that generates magenta, this

Table 3.2: Results of the optimization of planar and structured cells, for magenta (255, 0, 255) and green (0, 255, 0): values of FoM, as defined by Equation (2.7), J_{SC} and respective RGB colours, along with the optimal geometry parameters and corresponding size accurate illustrations (considering a cell base 1 μm^2), where the thicknesses of the LT, ITO and Spiro layers are represented as h, t_{ITO} and t_{Spiro}, respectively.

Illustration	PSO results	Illustration	PSO results
 (255, 44, 239)	FoM = 117.11 A/m^2 J_{SC} = 20.69 mA/cm^2 **J_{SC} gain = 0.00%** t_{ITO} = 157.72 nm t_{Spiro} = 108.45 nm	 (65, 255, 93)	FoM = 72.85 A/m^2 J_{SC} = 20.04 mA/cm^2 **J_{SC} gain = −3.14%** t_{ITO} = 216.22 nm t_{Spiro} = 200.00 nm
 (246, 12, 255)	FoM = 213.95 A/m^2 J_{SC} = 21.40 mA/cm^2 **J_{SC} gain = 3.44%** Pitch = 100.00 nm Width = 0.36 h = 116.18 nm t_{ITO} = 168.28 nm t_{Spiro} = 105.84 nm	 (17, 255, 60)	FoM = 142.76 A/m^{2*} J_{SC} = 20.58 mA/cm^2 **J_{SC} gain = −0.62%** Pitch = 275.06 nm Width = 0.57 h = 113.64 nm t_{ITO} = 118.50 nm t_{Spiro} = 198.13 nm
 (243, 9, 255)	FoM = 217.60 A/m^2 J_{SC} = 21.76 mA/cm^2 **J_{SC} gain = 5.18%** Pitch = 365.46 nm Width = 0.33 h = 112.92 nm t_{ITO} = 77.63 nm t_{Spiro} = 101.78 nm	 (7, 255, 29)	FoM = 210.62 A/m^{2*} J_{SC} = 21.06 mA/cm^2 **J_{SC} gain = 1.79%** Pitch = 100.00 nm Width = 0.33 h = 71.25 nm t_{ITO} = 169.40 nm t_{Spiro} = 200.00 nm
 (255, 4, 241)	FoM = 218.32 A/m^2 J_{SC} = 21.83 mA/cm^2 **J_{SC} gain = 5.52%** Pitch = 449.36 nm Radius = 0.35 h = 134.81 nm t_{ITO} = 155.95 nm t_{Spiro} = 100.03 nm	 (13, 255, 7)	FoM = 211.77 A/m^2 J_{SC} = 21.18 mA/cm^2 **J_{SC} gain = 2.37%** Pitch = 300.67 nm Radius = 0.35 h = 93.22 nm t_{ITO} = 176.98 nm t_{Spiro} = 192.56 nm
 (254, 0, 255)	FoM = 220.66 A/m^2 J_{SC} = 22.07 mA/cm^2 **J_{SC} gain = 6.68%** Pitch = 454.97 nm Radius = 0.39 Z radius = 357.73 nm t_{ITO} = 96.04 nm t_{Spiro} = 108.35 nm	 (13, 255, 7)	FoM = 213.96 A/m^2 J_{SC} = 21.40 mA/cm^2 **J_{SC} gain = 3.44%** Pitch = 250.00 nm Radius = 0.49 Z radius = 247.98 nm t_{ITO} = 50.00 nm t_{Spiro} = 200.00 nm

*Colour limit increased to 30.

colour was easier to achieve in the cells (in some cases, even with different geometries), and even corresponded to higher merit values, as clearly represented in Figure 3.15(b). In fact, although green only encompasses one reflection peak in the visible spectrum, the PSO algorithm struggled to find an optimal geometry, particularly in cells with linear and crossed gratings. Regarding the ability to preserve the current density enhancement provided by the LT features, Figure 3.15(b) introduces the J_{SC} gain values, relative to the reference cell, where magenta domes seem to have reached the maximum gain (6.68%) whilst green simple gratings were the only structure to result in a loss (-0.62%). Generally, according to these results, the best structures tested in this study, for the selected colours, at a normal light incidence angle, were nanopillars and domes, which resulted, overall, in higher J_{SC} and best chromaticities.

3.4 Angular uniformity

As colour is a result of a series of interferences of light that is redirected to the exterior, the angle of incidence, θ, is relevant for the subsequent refraction, scattering and diffraction angles, among other phenomena in the layers of the cells. Analogously, these same occurrences affect the optical and electrical performances of the cells, possibly redefining the quality of the cells entirely.

Considering the intended application of this technology, it is interesting to explore how different angles of light incidence might affect the chromaticity of the solar cells, as colour consistency is expected in BIPV. To this effect, the previously optimized solar cells were simulated with a plane wave source, injected at a variety of angles, while recording the corresponding chromaticity, J_{SC} and FoM progress. Figure 3.16 shows the transformed characteristics of the optimal magenta and green cells, for θ between 0° and 60°, with a step of 10°. Figure 3.16 has two different result categories, per structure: the chromaticity variation, depicted in CIE gamuts, throughout the angles (marker size increases with angle) and a polar plot that depicts the discrepancy of the unpolarized J_{SC} and FoM values at different θ values.

Good angular uniformity is also considered a merit attribute in this work, so it is important to compare the different cell performances, from Figure 3.16, as follows.

Despite their usually high angular sensitivity, the planar cells showed fairly good colour uniformity throughout the source inclination, compared to the optically enhanced alternatives. Such result might be explained by their highly intense reflection peaks in flat configurations (around 20%, in Figure 3.8(c)), in contrast to the remaining cells (lower than 10%, in Figures 3.11, 3.14, B.7 and B.4) — in lower reflection peaks, the smallest shift or reduction is likely to cause a transition to white, as seen for most LT enhanced cells. In the optimal flat cells, the magenta shade shifted to pink, and the green shade to white. Regarding J_{SC} divergence, a decrease of $\sim 1.3\,mA/cm^2$ was registered for both coloured cells, corresponding to a loss of $\sim 6\%$. However, this decline was not continuous throughout the angle increase, which is not abnormal in this study, as the cells had been

previously optimized for colour, and not only J_{SC}. As for the FoM, the magenta cell showed more decay, with a decrease of 56.93 A/m^2, as it presented a higher value initially. The merit decline in both cells was consistent with the increase of θ, due to colour degradation.

The optical angular dependency observed for all the optimal cells with LT features showed more degradation of the merit values, possibly due to their low reflection peaks at the relevant wavelengths, as previously mentioned. In the cells with linear and crossed gratings, there was a direct shift from the initial cell colours to white. In these configurations, the J_{SC} variations were identical, regardless of colour, with a maximum decline of 1.45 mA/cm^2 (6.47% relative loss), for the green cell; however, the FoM of the magenta cells suffered a larger decrease ($\sim$ 150 A/m^2 for both gratings), justified by the overall low FoM of the green cells (optimizations were not able to find the demanded green RGB).

Regarding domes and circular nanopillars, the green cells reflection peak suffered a shift to blue wavelengths, following its dissipation to create white colour; the magenta cells reflection peak in the blue region dissipated first, creating a shift to red/orange chromaticities, after which the peak at red wavelengths also extinguished, generating white. For both configurations, the FoM and J_{SC} decreased, as θ increased, a total of $\sim$ 165 A/m^2 and $\sim$ 1.3 mA/cm^2 (up to $\sim$ 6% loss), respectively.

Despite the best colour uniformity corresponding to planar cells, out of all the configurations, it still exhibited the lowest FoM and J_{SC} values at every angle, presenting minimal values at 60°, of 42.27 A/m^2 and 18.53 mA/cm^2, respectively. Domes and nanopillars had the most decrease in FoM, followed by crossed gratings and linear gratings. At 60°, the highest J_{SC} was attained for magenta domes (20.85 mA/cm^2) and the best FoM for magenta crossed gratings (63.18 A/m^2).

The colour instability observed in cells with photonic features, compared to flat configurations, is not in accord with literature. It is believed that this is due to the nature of the method, that does not regard the colour luminosity. As such, the geometries of the enhanced solar cells converged to exhibit minor reflection peaks, to maximize J_{SC}, despite the resulting colour brightness. As a consequence, the slightest change in θ results in the reduction, or even extinction, of these peaks, and drastic colour divergences.

Nevertheless, the colour fluctuation obtained for different incidence angles can be viewed as a compelling aspect for the aesthetics of numerous products, providing a holographic-like effect.

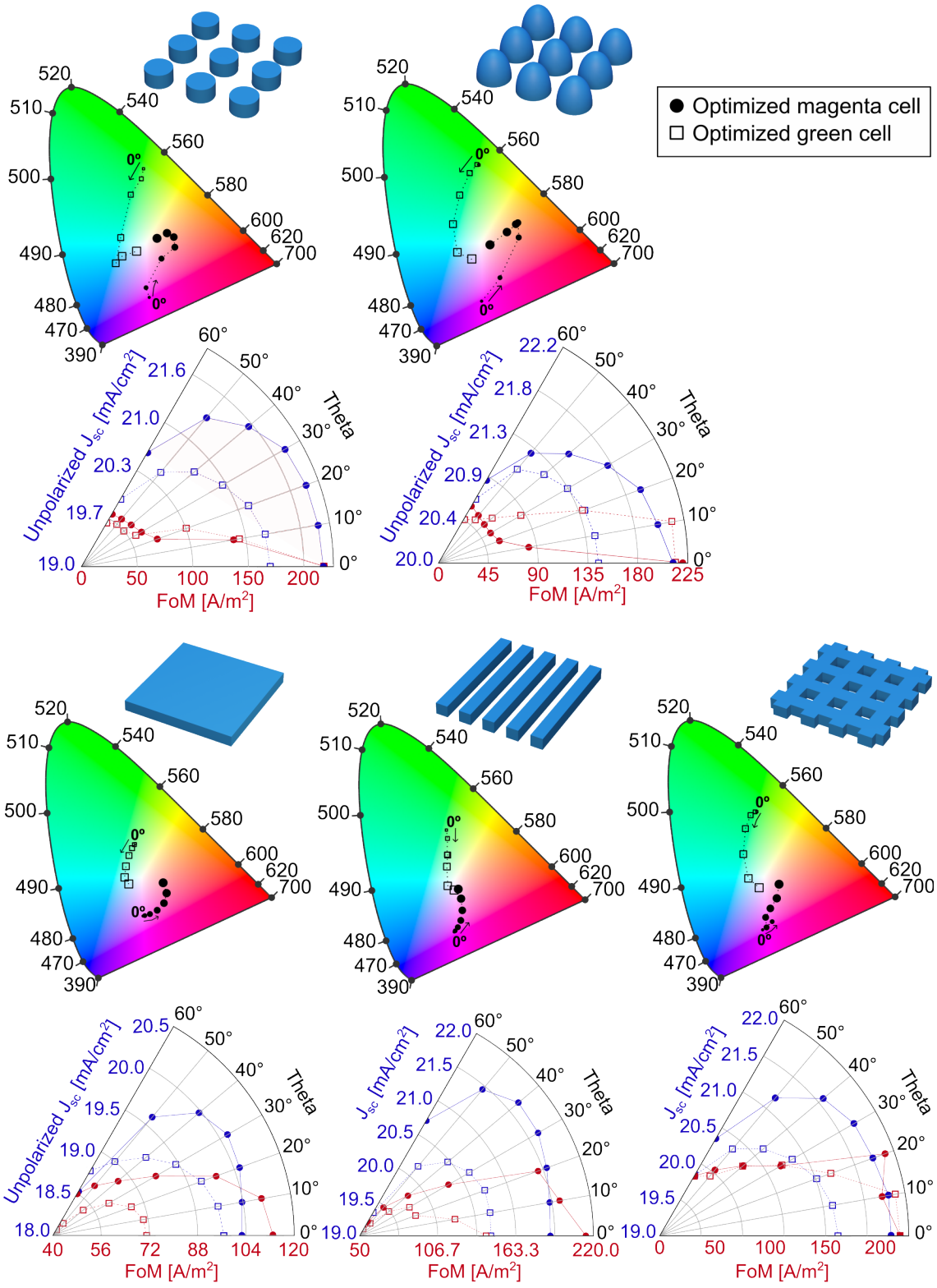


Figure 3.16: Solar cell chromaticity (shown in CIE gamut), unpolarized J_{SC} and FoM (shown in polar plots) for the optimal magenta and green cells in planar layout and with the photonic structures (illustrations represented accordingly). The incident angles of illumination (θ) varied between 0° and 60°, with a step of 10°. In the CIE gamuts, the scatter marker size increases along with the angle.

4 Conclusion and future perspectives

This project developed a computational method capable of optimizing any solar cell layout, to reflect selected frequencies and generate certain colours, while conserving its optical quality. In this procedure, the system takes the range of geometrical parameters of a certain cell configuration and the chosen RGB as input, and generates a solar cell with a specific layout that validates the requisites.

This method was tested by simulating and obtaining relevant optical performance attributes of different photonic geometries, shapes and symmetries, on top of $MAPbI_3$ solar cells (1.55 eV bandgap). Linear gratings, crossed gratings, circular nanopillars and domes were simulated, to test how the merit properties responded to different dimensional variables. Preliminarily, by simulating the flat configuration of the PSCs, it was found that the gradient of the ITO layer's height was sufficient to generate a variety of colours. Similarly, when sweeping through different values of the parameters of crossed gratings, the height of these structures revealed to be particularly crucial for colour selection. This height/hue relation became less relevant in linear gratings and circular nanopillars, and nonexistent for domes, but could become an interesting advantage in an industrial viewpoint, as a variety of coloured cells could be produced simply by selecting this particular parameter. After these observations, it became interesting to test how this colour variation is related to the effective refractive index of the photonic-enhancing layers, particularly for crossed gratings. It was found that, for this configuration, as well as circular nanopillars, the effective refractive index (hence, the unit cell volume ratio occupied by the structures) played most part in colour generation, for small structures. As the structures increased in size, their remaining geometrical features became more relevant in the selection of reflection peaks. Despite this relation, all geometrical parameters had a strong influence on J_{SC}, which highlighted the necessity to optimize the layout of the cells.

In the following step, the cells' layout were optimized to generate magenta and green cells, to test the reflection peaks at red, green and blue wavelengths (primary colours of the sRGB colour system employed in this work). It was observed that, overall, the magenta cells presented higher FoM and J_{SC} and the colour was more commonly achieved by the PSO. In fact, the green linear and crossed gratings cells were not able to converge to results that generated chromaticities within the demanded RGB range.

Regarding the differences observed between structures, the planar cell exhibited the lowest FoM, J_{SC} and highest RGB distances. By this point of the study, it is clear that the addition of LT features exhibit benefits regarding the colour and current generation. For the remaining cells, it was possible to declare that the best structures, at a normal light incidence angle, were circular nanopillars and domes, which were able to present the highest merit values (up to 220.7 A/m^2 – 6.68% gain, relative to the reference), the best optical performances and easily found the geometrical features that resulted in the demanded chromaticity.

With respect to the results of the optimal layout parameters, some similarities were

found among structures: generally, the heights of the planar layers converged to higher values for green cells, compared to magenta cells, and the size of the LT features was larger for magenta cells (linear gratings were the exception). It was also found that the values of pitch and height were somewhat similar for each colour. These agglomerates of pitch, LT height and planar layer thicknesses are compelling for production value, since this system can be simplified to the concept that certain geometrical ranges are likely to produce certain colours. Although this study does not encompass enough results to define such ranges, it introduces an interesting approach to tune structural colour.

Following the optimization of the solar cells, the angular uniformity test resulted in an unanticipated outcome, as the colour variance observed in cells with photonic features was more pronounced than in flat configurations; the colour changing aspect may be interpreted as a positive feature for some applications. Domes and nanopillars had the most decrease in FoM, followed by crossed gratings and linear gratings, but planar cells continued to exhibit the lowest FoM and J_{SC} values, at every angle.

The expectation is that future studies might improve the fine-tuning of the optimal cell geometries, to the point of their incorporation in practical work. In particular, a necessary alteration is to implement the luminosity of the colour, either by including the intensity of the reflection peaks in the FoM or by using a colour system that incorporates this quantity. The angular stability is a property that also requires further analysis, possibly by optimizing the cells for higher levels of luminosity, or by creating a new FoM variable that minimizes the colour dispersion throughout the inclination. Due to the adaptability of the method, semi-transparent solar cells, generally applied in windows, can be equally colour tuned, by combining the monitoring of the reflected and the transmitted light in the simulation object. On another note, the optimization methodology adopted in this work, the performance of multiple PSOs, might not be the best algorithm for search spaces with such complexity. Species-based PSO algorithm is a possible alternative, where the particles focus on finding a variety of local maxima, instead of following one "leader" particle with the best position in the space, possibly disregarding multiple variable combinations. By adopting this method, the optimization time reduces, and the particles are more likely to find the global maxima [40]. Regarding the future manufacturing of this technology, multiple nanofabrication techniques are compatible with the structures of this work, such as soft-lithography processes, particularly colloidal lithography [41].

Overall, it may be said that this work has achieved compatibility between opposite physical effects, by computational optimization, by applying colour to solar cells (which originates an optical loss), while guaranteeing the generation of the maximum feasible short circuit current density. The manufacturing and eventual commercialization of this technology has the potential to further exploit solar power directly in consumer-oriented products, where an aesthetic component is important.

Bibliography

[1] J. M. Lourenço. *The NOVAthesis Template User's Manual*. NOVA University Lisbon. 2021. URL: https://github.com/joaomlourenco/novathesis/raw/main/template.pdf (cit. on p. i).

[2] *Solar - IEA*. URL: https://www.iea.org/energy-system/renewables/solar-pv#tracking (visited on 2023-08-04) (cit. on p. vii).

[3] A. Paulet. *Building-integrated Photovoltaics Market Size Report, 2030*. URL: https://www.grandviewresearch.com/industry-analysis/building-integrated-photovoltaics-bipv-market# (visited on 2023-08-04) (cit. on p. vii).

[4] T. M. Koh et al. "Halide Perovskite Solar Cells for Building Integrated Photovoltaics: Transforming Building Façades into Power Generators". In: *Advanced Materials* 34 (25 2022-06). DOI: 10.1002/adma.202104661 (cit. on pp. vii, 1, 3, 4).

[5] *Building Integrated Photovoltaics*. URL: https://www.ise.fraunhofer.de/en/key-topics/integrated-photovoltaics/building-integrated-photovoltaics-bipv.html (visited on 2023-10-06) (cit. on p. vii).

[6] *National Renewable Energy Laboratory (NREL) Home Page | NREL*. URL: https://www.nrel.gov/ (visited on 2023-10-06) (cit. on p. vii).

[7] M. A. Green et al. "Solar cell efficiency tables (version 62)". In: *Progress in Photovoltaics: Research and Applications* (2023-07). DOI: 10.1002/pip.3726 (cit. on p. 1).

[8] C. S. Schuster et al. "Empowering Photovoltaics with Smart Light Management Technologies". In: Springer New York, 2021, pp. 1–84. DOI: 10.1007/978-1-4614-6431-0_112-1 (cit. on pp. 1–5).

[9] S. Haque et al. "Photonic-structured TiO2 for high-efficiency, flexible and stable Perovskite solar cells". In: *Nano Energy* 59 (2019-05), pp. 91–101. DOI: 10.1016/J.NANOEN.2019.02.023 (cit. on pp. 1, 2, 7).

[10] T. M. Brenner et al. "Hybrid organic—inorganic perovskites: low-cost semiconductors with intriguing charge-transport properties". In: *Nature Reviews Materials 2016 1:1* 1 (1 2016-01), pp. 1–16. DOI: 10.1038/natrevmats.2015.7 (cit. on p. 1).

[11] H. Zhu et al. "Long-term operating stability in perovskite photovoltaics". In: *Nature Reviews Materials 2023 8:9* 8 (9 2023-08), pp. 569–586. DOI: 10.1038/s41578-023-00582-w (cit. on p. 1).

[12] E. Unger and T. J. Jacobsson. "The Perovskite Database Project: A Perspective on Collective Data Sharing". In: *ACS Energy Letters* 7.3 (2022), pp. 1240–1245. DOI: 10.1021/acsenergylett.2c00330 (cit. on p. 1).

[13] J. H. Noh et al. "Chemical management for colorful, efficient, and stable inorganic-organic hybrid nanostructured solar cells". In: *Nano Letters* 13 (4 2013). DOI: 10.1021/nl400349b (cit. on p. 1).

[14] H. Zhu et al. "Efficient and Stable Large Bandgap MAPbBr3 Perovskite Solar Cell Attaining an Open Circuit Voltage of 1.65 V". In: *ACS Energy Letters* 7.3 (2022-03), pp. 1112–1119. DOI: 10.1021/acsenergylett.1c02431 (cit. on p. 1).

[15] M. J. Mendes et al. "Optimal-Enhanced Solar Cell Ultra-thinning with Broadband Nanophotonic Light Capture". In: *iScience* 3 (2018-05), pp. 238–254. DOI: 10.1016/j.isci.2018.04.018 (cit. on p. 2).

[16] K. Li et al. "Light trapping in solar cells: simple design rules to maximize absorption". In: *Optica, Vol. 7, Issue 10, pp. 1377-1384* 7 (10 2020-10), pp. 1377–1384. DOI: 10.1364/OPTICA.394885 (cit. on pp. 2, 13).

[17] T. K. Chong et al. "Optimal wavelength scale diffraction gratings for light trapping in solar cells". In: *Journal of Optics* 14 (2 2012-01), p. 024012. DOI: 10.1088/2040-8978/14/2/024012 (cit. on p. 2).

[18] O. Sanchez-Sobrado et al. "Lightwave trapping in thin film solar cells with improved photonic-structured front contacts". In: *Journal of Materials Chemistry C* 7 (21 2019-05), pp. 6456–6464. DOI: 10.1039/C8TC06092D (cit. on p. 3).

[19] O. Sanchez-Sobrado et al. "Photonic-structured TCO front contacts yielding optical and electrically enhanced thin-film solar cells". In: *Solar Energy* 196 (2020-01), pp. 92–98. DOI: 10.1016/J.SOLENER.2019.11.051 (cit. on p. 3).

[20] J. Halme et al. "Theoretical efficiency limits of ideal coloured opaque photovoltaics". In: *Energy and Environmental Science* 12 (4 2019), pp. 1274–1285. DOI: 10.1039/C8EE03161D (cit. on p. 4).

[21] Y. Jiang et al. "Efficient Colorful Perovskite Solar Cells Using a Top Polymer Electrode Simultaneously as Spectrally Selective Antireflection Coating". In: *Nano Letters* 16 (12 2016-12), pp. 7829–7835. DOI: 10.1021/acs.nanolett.6b04019 (cit. on p. 4).

[22] J. Li et al. "Highly Efficient Thermally Co-evaporated Perovskite Solar Cells and Mini-modules". In: *Joule* 4 (5 2020-05), pp. 1035–1053. DOI: 10.1016/j.joule.2020.03.005 (cit. on p. 4).

[23] A. Røyset, T. Kolås, and B. P. Jelle. "Coloured building integrated photovoltaics: Influence on energy efficiency". In: *Energy and Buildings* 208 (2020-02). DOI: 10.1016/j.enbuild.2019.109623 (cit. on p. 4).

[24] K. T. Lee et al. "Highly Efficient Colored Perovskite Solar Cells Integrated with Ultrathin Subwavelength Plasmonic Nanoresonators". In: *Scientific Reports* 7 (1 2017-12). DOI: 10.1038/s41598-017-10937-3 (cit. on p. 4).

[25] G. Peharz et al. "Application of plasmonic coloring for making building integrated PV modules comprising of green solar cells". In: *Renewable Energy* 109 (2017), pp. 542–550. DOI: 10.1016/j.renene.2017.03.068 (cit. on p. 4).

[26] H. A. MacLeod. *Thin-Film Optical Filters*. CRC Press, 2001-01, p. 641. ISBN: 9780429146053. DOI: 10.1201/9781420033236 (cit. on p. 4).

[27] J. C. O. Lizcano et al. "Optimal Design of Multilayer Optical Color Filters for Building-Integrated Photovoltaic (BIPV) Applications". In: *Solar RRL* (2023). DOI: 10.1002/solr.202300256 (cit. on p. 4).

[28] G. Y. Yoo et al. "Stable and Colorful Perovskite Solar Cells Using a Nonperiodic SiO2/TiO2 Multi-Nanolayer Filter". In: *ACS Nano* 13 (9 2019-09), pp. 10129–10139. DOI: 10.1021/acsnano.9b03098 (cit. on p. 4).

[29] J. Rao and S. Varlamov. "Light trapping in thin film polycrystalline silicon solar cell using diffractive gratings". In: *Energy Procedia* 33 (2013), pp. 129–136. DOI: 10.1016/j.egypro.2013.05.049 (cit. on p. 5).

[30] D. H. Cho et al. "Colorful solar cells utilizing off-axis light diffraction via transparent nanograting structures". In: *Nano Energy* 80 (2021-02). DOI: 10.1016/j.nanoen.2020.105550 (cit. on p. 5).

[31] F. F. Mahani and A. Mokhtari. "TiO2 Circular Nano-Gratings as Anti-Reflective Coatings and Potential Color Filters for Efficient Organic Solar Cells". In: *Journal of Nanoelectronics and Optoelectronics* 13 (11 2018-12), pp. 1624–1629. DOI: 10.1166/jno.2018.2412 (cit. on p. 5).

[32] D. M. Sullivan. *Electromagnetic Simulation Using the FDTD Method*. John Wiley and Sons, Ltd, 2013. ISBN: 9781118646700. DOI: https://doi.org/10.1002/9781118646700.ch1 (cit. on pp. 6, 50, 51).

[33] *Ansys Lumerical FDTD Learning Track Ansys Courses*. URL: https://courses.ansys.com/index.php/learning-track/ansys-lumerical-fdtd/ (visited on 2023-08-04) (cit. on pp. 6, 51).

[34] M. J. Mendes et al. "Design of optimized wave-optical spheroidal nanostructures for photonic-enhanced solar cells". In: *Nano Energy* 26 (2016-08), pp. 286–296. DOI: 10.1016/J.NANOEN.2016.05.038 (cit. on p. 6).

[35] *Converting a spectrum to a colour*. URL: https://scipython.com/blog/converting-a-spectrum-to-a-colour/ (cit. on pp. 8, 53, 54).

[36] X.-S. Yang. "Particle Swarm Optimization". In: *Nature-Inspired Optimization Algorithms* (2021-01), pp. 111–121. DOI: 10.1016/B978-0-12-821986-7.00015-9 (cit. on p. 8).

[37] L. M. Le et al. "Hybrid Artificial Intelligence Approaches for Predicting Buckling Damage of Steel Columns Under Axial Compression". In: *Materials 2019, Vol. 12, Page 1670* 12 (10 2019-05), p. 1670. DOI: 10.3390/MA12101670 (cit. on p. 8).

[38] M. R. Fialho. "Computational Design of Colourful and Flexible Photonic-enhanced Solar Cells". MA thesis. 2023. URL: http://hdl.handle.net/10362/153470 (cit. on pp. 9, 10, 17).

[39] M. Alexandre. *EM Software Repository*. https://github.com/perspe/em_methods. (Visited on 2023-09-23) (cit. on p. 11).

[40] K. Deb et al., eds. *Genetic and Evolutionary Computation - GECCO 2004, Genetic and Evolutionary Computation Conference, Seattle, WA, USA, June 26-30, 2004, Proceedings, Part II*. Vol. 3103. Lecture Notes in Computer Science. Springer, 2004. ISBN: 3-540-22343-6 (cit. on p. 33).

[41] S. Haque et al. "Design of wave-optical structured substrates for ultra-thin perovskite solar cells". In: *Applied Materials Today* 20 (2020-09), p. 100720. DOI: 10.1016/J.APMT.2020.100720 (cit. on p. 33).

[42] *RefractiveIndex.INFO - Refractive index database*. URL: https://refractiveindex.info/ (visited on 2023-09-20) (cit. on p. 49).

[43] J. B. Schneider. "Understanding the Finite-Difference Time-Domain Method". In: (2022). URL: www.eecs.wsu.edu/~schneidj/ufdtd (cit. on p. 51).

[44] C. Wyman, P.-P. Sloan, and P. Shirley. "Simple Analytic Approximations to the CIE XYZ Color Matching Functions". In: *Journal of Computer* 2 (2 2013) (cit. on p. 53).

[45] H. Fairman, M. Brill, and H. Hemmendinger. "How the CIE 1931 color matching functions were derived from Wright Guild data". In: *Color Research Application* 22.1 (1997), pp. 11–23 (cit. on p. 53).

[46] *What is the CIE Color Space? What's the difference between CIE 1931 and CIE 1976? – Luminus Devices*. URL: https://luminusdevices.zendesk.com/hc/en-us/articles/4414846186253-What-is-the-CIE-Color-Space-What-s-the-difference-between-CIE-1931-and-CIE-1976- (visited on 2023-08-20) (cit. on p. 55).

A FDTD setup and convergence tests

The simulation region is defined as the unit cell, to which periodic boundary conditions were applied, in the x and y directions. Additionally, when the structures presented symmetry, the x and y boundaries were both periodic and symmetric/anti-symmetric, which reduces the computation time by 4 times. The FDTD solver defines perfectly matched layers (PML) as boundary conditions in the z direction of the unit cell, in order to prevent reflection of the waves in the structural limits. These boundaries act as absorbing barriers and match the impedance to the surrounding materials, to avoid unrealistic reflections.

As mentioned in Annex II, the electric and magnetic fields are calculated at each mesh node. By default, the automatically created mesh of the FDTD solver region (auto non-uniform default setting) is smaller in high refraction index zones, because the wavelength is smaller in these materials. In solar cell simulations, it is common to add supplementary small meshing grids to obtain more accurate results, specifically around complex structures, where the fields vary drastically. In this work, two additional rectangular Cartesian meshes were used, and their sizes depended on the required resolution: a smaller mesh enables higher accuracy, at the cost of simulation time and memory. One of these meshes, referred as "top mesh" in Figure 2.1, included the LT region, the ITO and SnO_2 planar layers and the top 80 nm of the perovskite layer. This improves the accuracy in the interfaces of the top layers and on the photocurrent density calculated in the perovskite region, as well as in the complex geometry regions of the LT features. Another mesh was placed in the perovskite/Spiro-OMeTAD interface, referred as "bottom mesh". The process of determining the best specifications for the supplementary and solver region meshes are explained in the following Sections, A.1 and A.2, for normal and oblique incident angles, respectively.

The simulation model also included a planar wave source, that injects a Gaussian beam to the cell, from the LT side. The propagation direction was defined as normal to the surface and the polarization angle was set to 0°(P-polarized), for the optimization of all the structures except grating lines. As previously mentioned, grating lines are commonly placed on top of solar cells, due to their simple production and adaptability, but a significant disadvantage of these structures are their one-dimensionality, which cannot be correctly simulated with only one light polarization. Hence, it was necessary to simulate these cells with two different source settings: P-polarization (polarization angle = 0°) and S-polarization (polarization angle = 90°). For this configuration, the photocurrent density and reflection spectra of the cell corresponds to the mean estimate of the results of both polarizations.

As for the study of how different incidence angles affect the chromaticity and J_{SC} of the cells, the FDTD settings had to be adapted. An oblique incident angle can be selected by changing the angle theta (in respect to the z axis) in the plane source. In these simulations, the x and y boundary conditions of the FDTD simulation region were set to Bloch, which

takes into account the field's phase change across each period, unlike periodic boundaries. However, non-null incident angles are associated with a series of numeric errors, which lead to the necessity of another convergence test, further explained in appendix A.2.

In order to determine the colour of the cell, it is necessary to attain the reflection spectrum by a frequency-domain profile and power monitor placed on top of the cell. The number of frequency points at which the data is recorded may have a substantial impact on the spectrum and, as a consequence, may have some influence on the precision of the colour estimation. This number was set to 81, which is a good compromise between precision and computation time.

A.1 Convergence test: FDTD simulations at normal angle of illumination

In order to increase memory efficiency, by minimizing the duration of the simulations, whilst maintaining the quality of the results, a convergence test was made. To carry out this test, three parameters were accounted for: the equivalent refractive index of the mesh override region (defined in the additional meshes), the global mesh accuracy and the amount of PML layers of the FDTD boundaries (defined in the FDTD solution region), as these are some of the main restrictions regarding the speed and precision of simulations:

- Additional mesh regions: the mesh override regions can be used to specify an equivalent refractive index for the volume of a particular region. The mesh spacing is then determined by the equivalent index - a higher index will lead to a finer mesh and more accurate results.

- FDTD global mesh: when using the auto non-uniform mesh, a global mesh accuracy of 1 or 2 is used for fast simulations with low accuracy and low memory requirements. These accuracy levels are useful to run the first simulations more quickly, before refining the mesh. In a later stage, a mesh accuracy of 3 or 4 is a good tradeoff between accuracy, memory requirements and simulation time.

- PML layers: an ideal PML boundary absorbs the incident light, but, in reality, there will always be some reflection due to the discretization associated with the PML equations and consequent numerical instabilities. These reflections can be minimized by increasing the number of layers, which also increases the simulation time.

The best course of action to study the most optimal combination of these parameters involved a two-part process. The equivalent index of the top mesh region was tested uniformly in all dimensions, between $(x, y, z) = (3, 3, 3)$ and $(x, y, z) = (5, 5, 5)$, with a step of $\frac{1}{6}$, the bottom mesh index varied in the z direction between $(x, y, z) = (3, 3, 3)$ and $(x, y, z) = (3, 3, 5)$, with a step of $\frac{1}{6}$, and the global mesh accuracy assumed the values

of 1, 2, 3 and 4. The previous settings were tested for crossed gratings and for domes (the optimal FDTD setup of the domes was applied to the simulations of the nanopillars, as these correspond to a similar but simpler structures, and the same logic applies to linear and crossed gratings). Firstly, the influence of the accuracies of the two additional meshes were simultaneously tested through a double sweep. As a result of this sweep, it was possible to plot a 3D map of the photocurrent density as function of two axis, the equivalent top mesh index and equivalent bottom mesh index. These results can be observed in Figure A.1, where it is possible to conclude that the equivalent index of the bottom mesh has nearly no impact on the photocurrent density. Accordingly, the next step tested the global mesh accuracy and the equivalent index of the top mesh, as the equivalent index of the bottom mesh was fixed at $(x, y, z) = (3, 3, 3)$. The optimal mesh settings were selected, based on the area of the map where the result seemed to vary the least (indicating that the simulation settings and underlying numeric errors were least impactful on the results) while choosing the lowest accuracy within this area (as to minimize simulation time). According to this strategy, the equivalent top mesh index was set to $(x, y, z) = (4.333, 4.333, 4.333)$ and the global mesh accuracy was fixed at 3 for all structures, as per the results in Figure A.1. These parameters were later applied to the optimization scripts, as to guarantee decent accuracy, while minimizing simulation time.

The mesh settings selected through this process were obtained for a specific geometry for each structure. However, this configuration may not be applicable for different LT structure sizes. To quickly test different dimensions, each parameter was varied, according to the ranges defined for the optimizations, in order to check the auto shutoff level of the simulation. This factor is an estimate of the energy remaining in the FDTD region, as a fraction of the injected power. Once this fraction falls below a specified threshold (default is 10^5), the simulation ends, as the fields have run for enough time to decay. If the simulation does not trigger this early shutoff feature, it is likely that the simulation time was not sufficient for the fields to fully decay, leading to inaccurate results. This is a common occurrence when resonance phenomena are present in the device. In this work, resonance is most likely related to unwanted reflections in the FDTD boundaries, that can be reduced by increasing the amount of PML layers. The auto shutoff level was reached for all structures, for 16 PML layers, except in linear gratings, where it was necessary to increase this value to 32.

A.2 Convergence test: FDTD simulations at oblique angles of illumination

In planar wave sources, it is possible to vary two angles: θ (in relation to the z axis) and ϕ (in relation to the xy plane). For the particular structures simulated in this work, only the θ angular dependency was studied, as ϕ showed no relevancy in symmetric features.

The main causes of error in FDTD simulations with a plane wave source injected

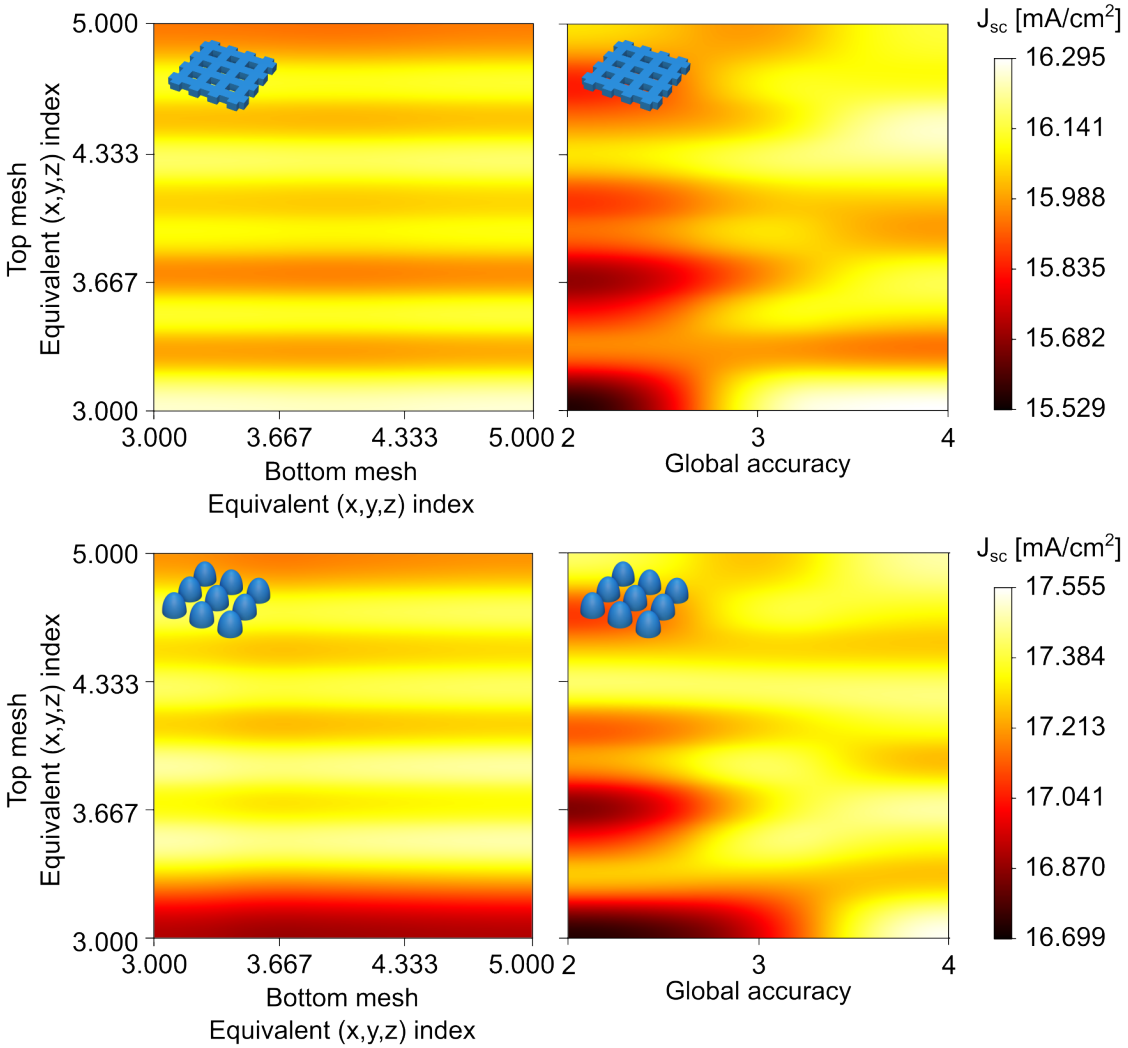


Figure A.1: Convergence test results: current density for different mesh configurations, for crossed grating and dome LT structures.

at an angle are related to PML reflections in the Bloch boundary conditions (which are more pertinent for higher θ) and wavelength dependence of the injection angles (and consequent formation of evanescent fields, when the effective incident angle is over 90°).

Since the real injection angle varies throughout frequency (according to Equation (A.1)), when performing a broadband simulation, the accuracy of the results decreases as the wavelength values become more distant from the center frequency of the source. To mitigate this issue, it was necessary to simulate each wavelength individually, which increased the simulation time significantly, particularly considering that the optical results are the arithmetic average of the values attained by P-polarized and S-polarized light. As such, only 3 values of θ were tested for convergence, 0°, 30° and 60°.

$$\theta(f) = \arcsin\left(\frac{\sin(\theta_{sim}) f_{sim}}{f}\right) \tag{A.1}$$

In Equation (A.1), θ_{SIM} is the nominal injection angle, f_{SIM} is the center frequency of the source, and $\theta(f)$ is the effective incident angle of the light at frequency f.

To minimize the computational requirements, while maintaining high accuracy, the mesh spacial resolution and amount of PML layers were adapted. The absorption in the perovskite layer, in flat cell configuration, obtained by the FDTD method is compared to the spectra attained by the analytical scattering matrix method. As seen in Figure A.2, the results from both methods are very similar, for P-polarized (TE) and S-polarized (TM) light, indicating good simulation accuracy. This was attained for a top mesh equivalent index of 4 and 16 "steep-angle" PML layers.

As the convergence test was performed for the planar configuration of the cells, for the cells with LT features, the top mesh equivalent index was increased to 4.5 and 32 steep-angle PML layers.

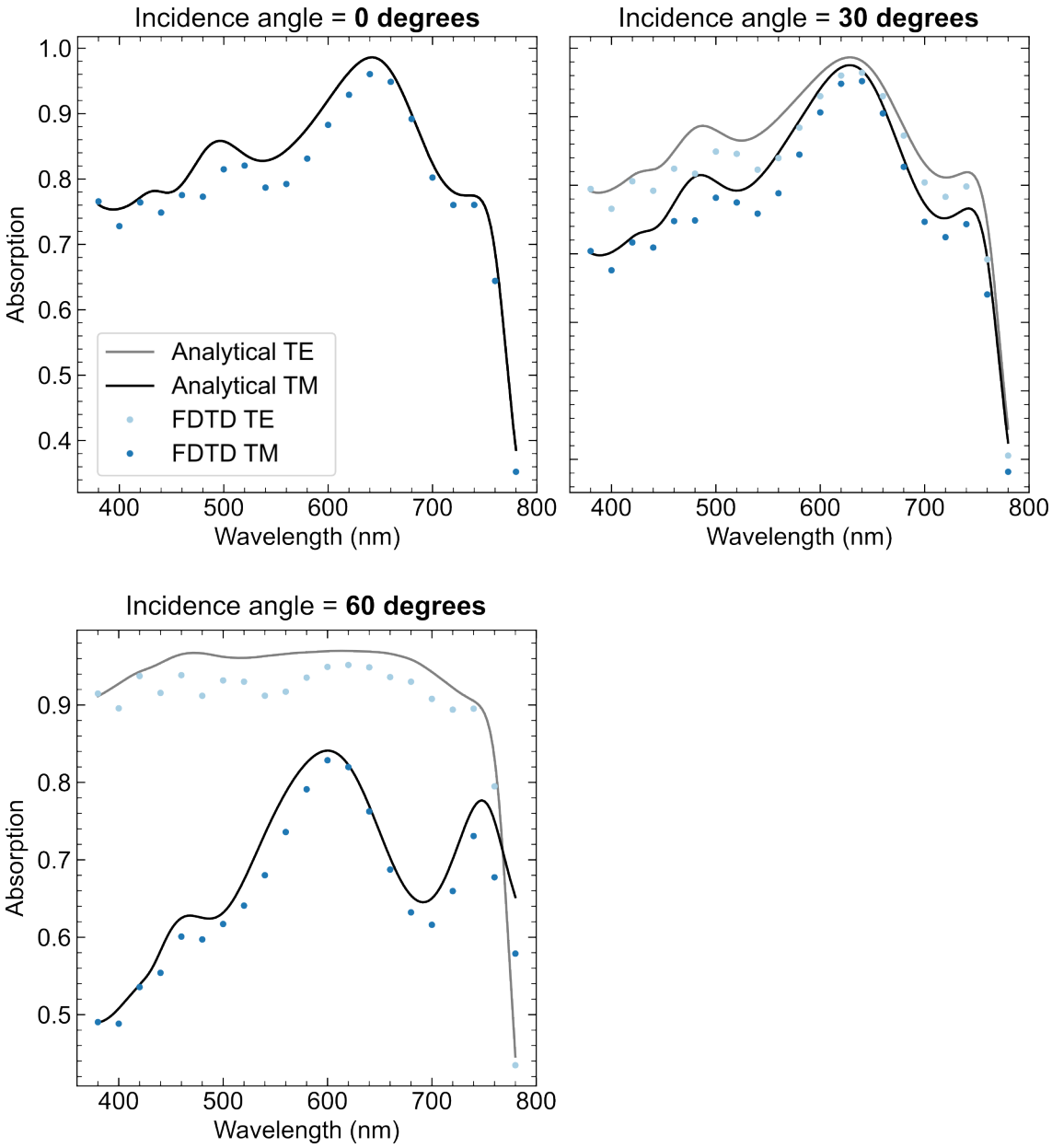


Figure A.2: Comparison between the perovskite absorption spectra of the flat cell configuration, obtained by the numeric FDTD method (scatter plots) and by the analytical scattering matrix method (line plots), for 0°, 30° and 60° incident angles of illumination, for P-polarized (TE) and S-polarized (TM) sources.

B Optimization results: grid plots

B.1 Reference cell

The reference cell was obtained by optimizing the flat configuration for maximum J_{SC}, where the only variables were the thicknesses of the ITO and Spiro layers. Multiple PSOs were performed, for a wide range of variables, followed by a narrow selected ranged. The results are present in the grid plots of Figure B.1, where the best FoM value corresponded to FoM = 206.89 A/m^2. This current density serves as an optical performance reference for the remaining optimizations.

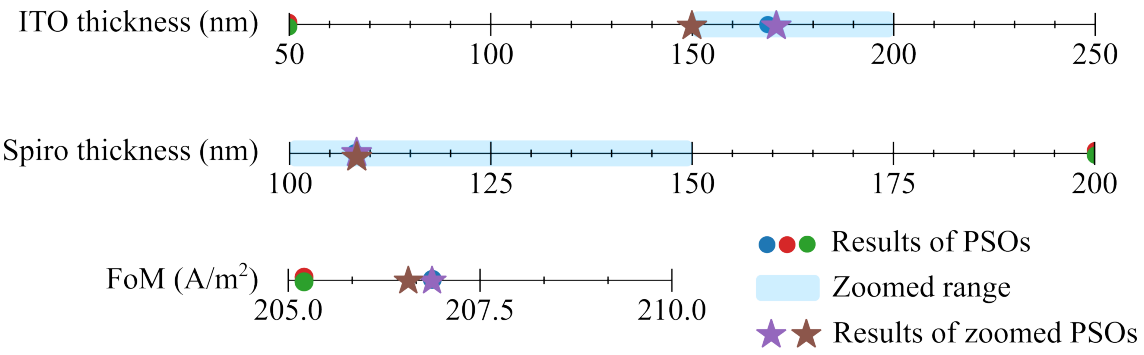


Figure B.1: Results of the optimization of the flat solar cell for the maximization of J_{SC} (for wide and zoomed variable ranges).

B.2 Circle nanopillars

The pitch, radius and height of circular nanopillars, as well as the heights of the planar ITO and Spiro layers, were optimized to present magenta (RGB = (255, 0, 255)) and green (RGB = (0, 255, 0)) colours. The results of the multiple PSOs, and subsequent results for zoomed parameter ranges, can be observed in Figures B.2 and B.3, for magenta and green, respectively.

The best merit values found in magenta solar cells were FoM = 218.32 A/m^2 and J_{SC} = 21.83 mA/cm^2 (5.52% current density gain, relative to the reference cell), for an RGB distance of 14.56. For the green cell, one of the wide-range PSOs was able to find geometries with RGB distances lower than the colour limit of the FoM, and the zoom parameter ranges were selected according to this result. The best configuration presented FoM = 211.77 A/m^2 and J_{SC} = 21.18 mA/cm^2 (2.37% current density gain, relative to the reference cell), for an RGB distance of 14.76.

With regard to the reflection spectra of the optimal magenta cell, Figure B.4 shows that the nanopillars promote significant absorption enhancement, but do not alter the position of the peaks. For green cells, the nanopillars also suppress the reflection peaks in red and

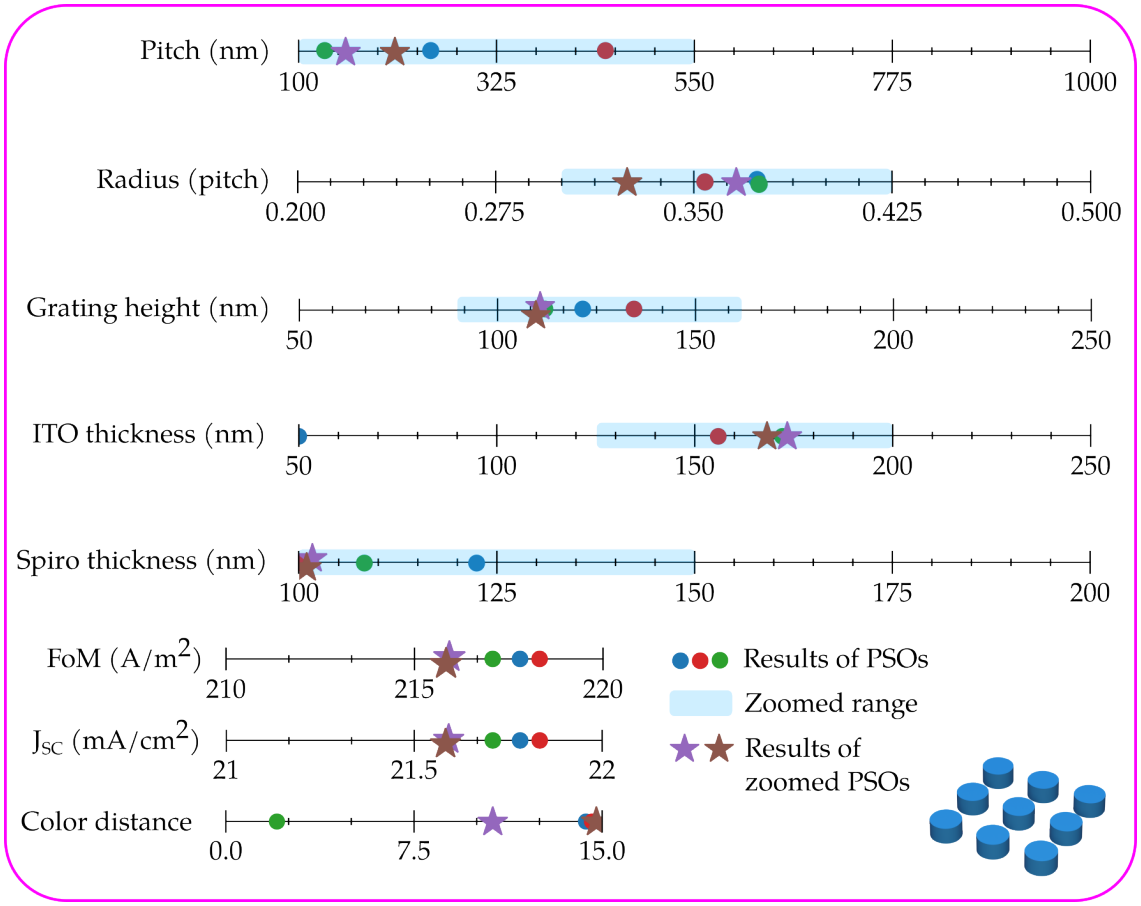


Figure B.2: Results of the optimization of magenta solar cells with circular nanopillars LT features: optimal geometrical parameters and respective FoM, J_{SC} and RGB distances for multiple PSOs, for wide and zoomed variable ranges.

blue wavelength regions, but not in the NIR region, possibly contributing for the lower value of J_{SC}, compared to the magenta cell.

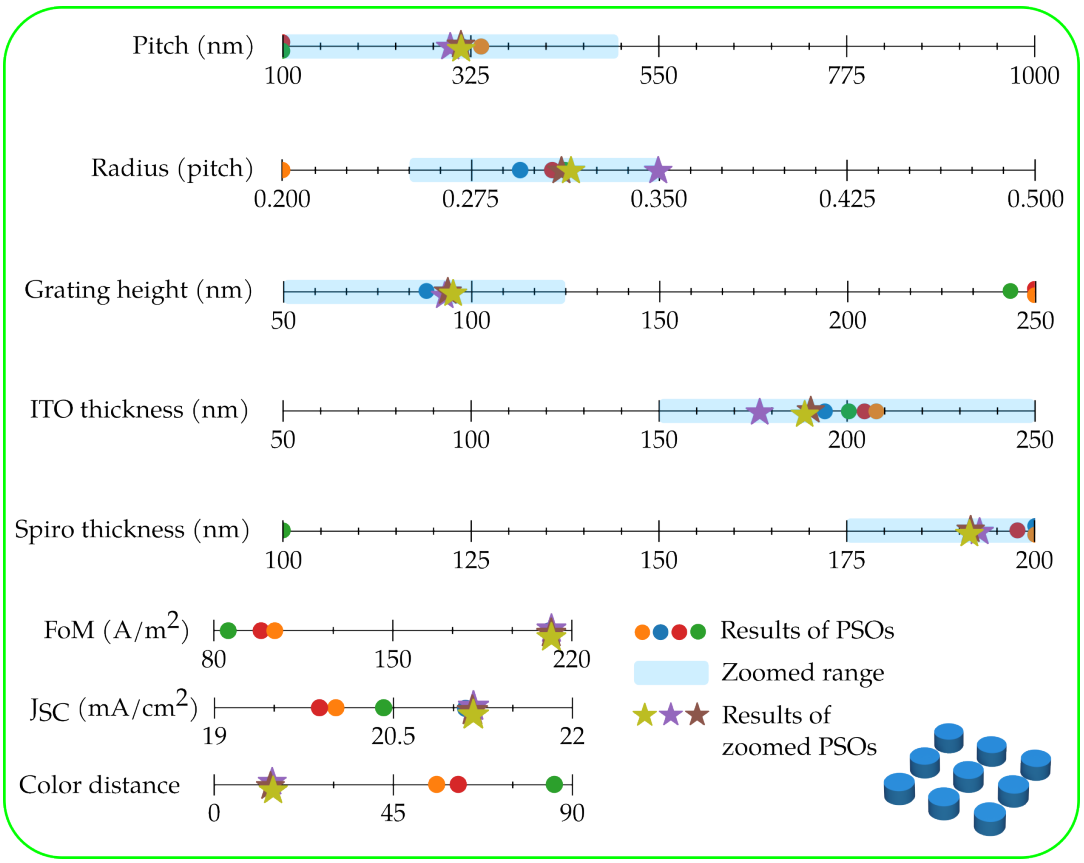


Figure B.3: Results of the optimization of green solar cells with circular nanopillars LT features: optimal geometrical parameters and respective FoM, J_{SC} and RGB distances for multiple PSOs, for wide and zoomed variable ranges.

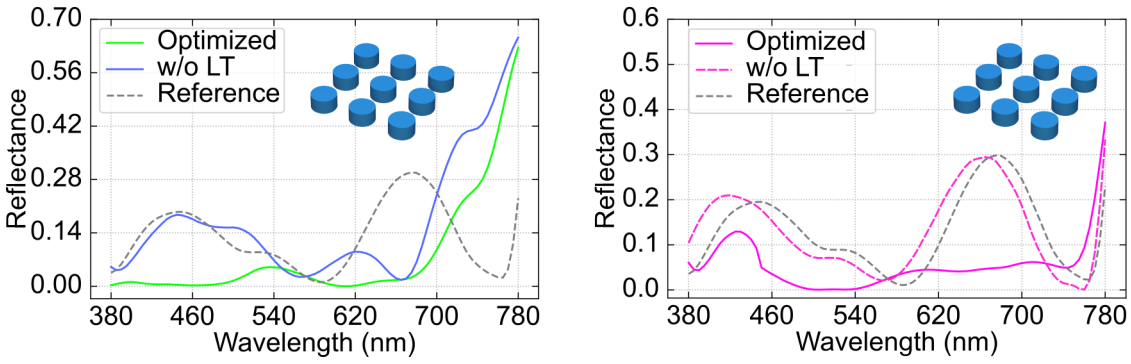


Figure B.4: Reflection spectra attained for optimal solar cells with circular nanopillars, with and without LT features, for green (left plot) and magenta (right plot), and respective reference spectrum. The solar cell colours were applied to each corresponding lines.

B.3 Linear gratings

Analogously, the pitch, width and height of linear gratings, as well as the thicknesses of the planar ITO and Spiro layers, were optimized multiple times, and the corresponding results are in Figures B.5 and B.6, for the generation of magenta and green, respectively.

When optimizing the cell with linear gratings to generate magenta, the best results were FoM = 213.95 A/m^2 and J_{SC} = 21.40 mA/cm^2 (3.44% current density gain, relative to the reference cell), for an RGB distance of 15, corresponding to the lowest merit values of the magenta cells, with LT features. Additionally, the PSOs' performance of the optimization of the green cell was even less satisfactory, since they were not able to find a cell layout that generated a colour within the admissible RGB values. Similarly to crossed gratings (Section 3.2.2), the colour limit of the FoM expression was increased to 30. Despite this change, the following PSOs were still not capable of reaching a high merit figure, due to RGB distances over 30. The best result indicated FoM = 142.76 A/m^2 and J_{SC} = 20.56 mA/cm^2 (0.62% current density loss), for an RGB distance of 62.36. This was the only configuration with LT structures that resulted in lower J_{SC} than the reference flat cell.

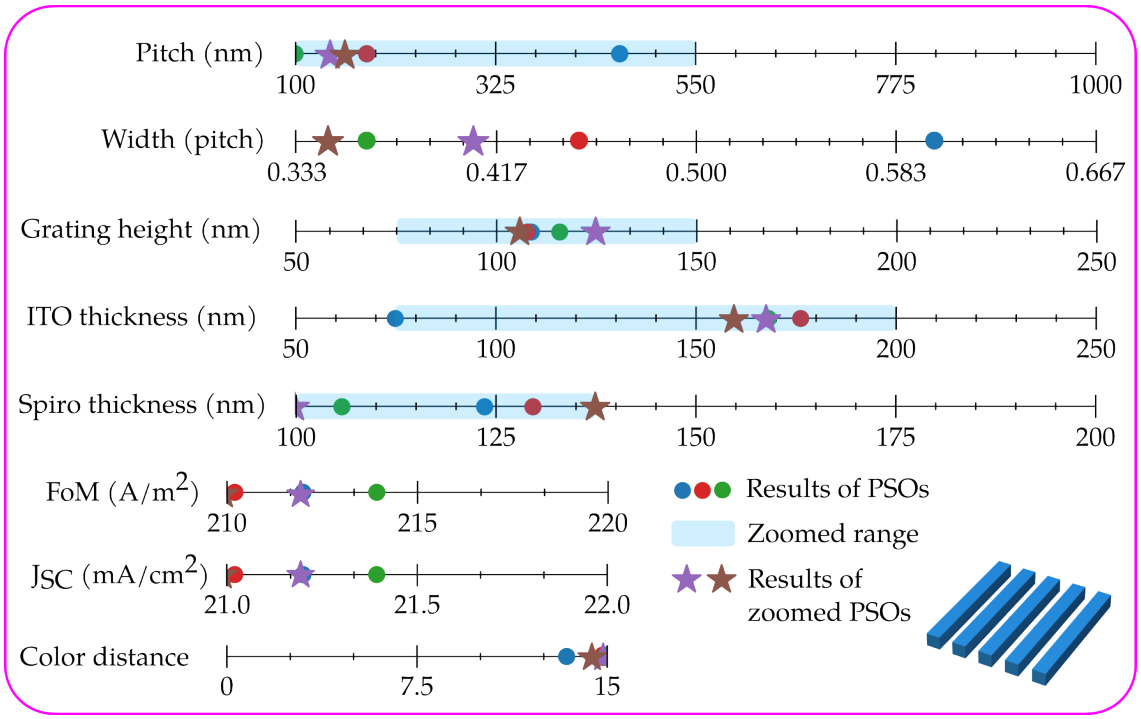


Figure B.5: Results of the optimization of magenta solar cells with linear gratings LT features: optimal geometrical parameters and respective FoM, J_{SC} and RGB distances for multiple PSOs, for wide and zoomed variable ranges.

The reflection spectra attained for the optimal solar cells with linear gratings, seen in Figure B.7, reveals the highest reflection peaks (~ 15%) of any other solar cell with LT features, which explains why this configuration presented the lowest J_{SC} values. An intriguing detail in the optimal magenta solar cell is that the thicknesses of the ITO and

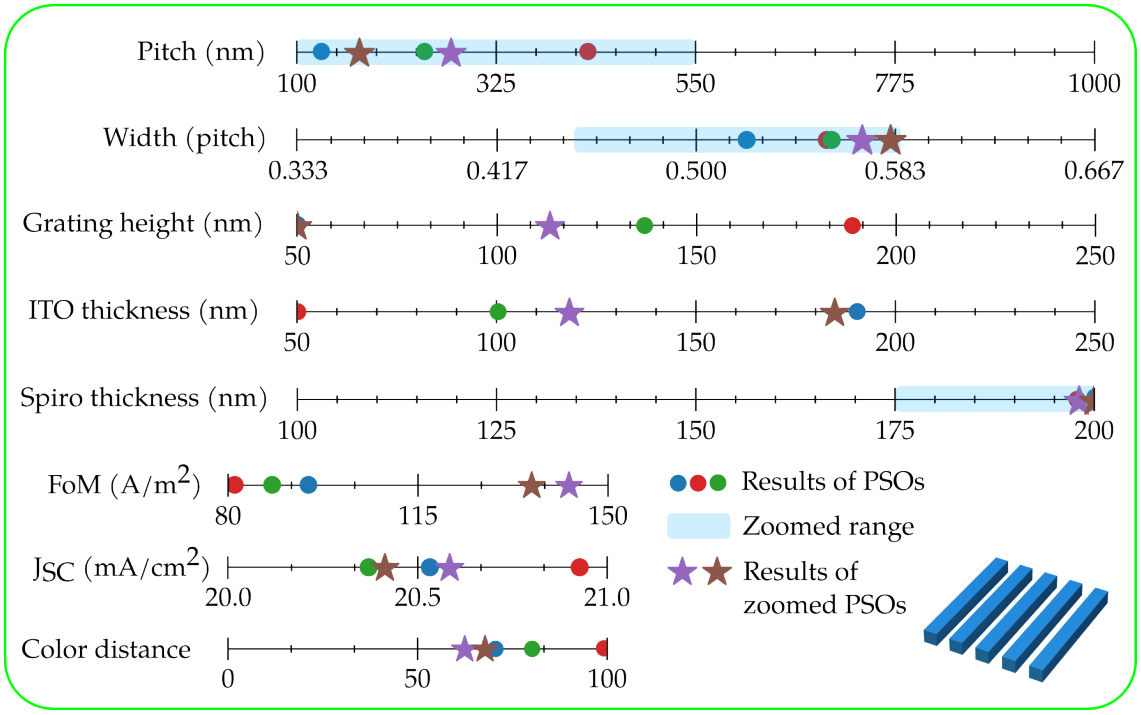


Figure B.6: Results of the optimization of green solar cells with linear gratings LT features: optimal geometrical parameters and respective FoM, J_{SC} and RGB distances for multiple PSOs, for wide and zoomed variable ranges.

Spiro layers converged to the same values as the reference cell (optimal layout of the flat cells, for maximum J_{SC}) and the linear gratings were able to reduce the intensity of the peaks, whilst filtering the green wavelengths. The green cell was not able to completely decrease the reflection in the blue and red wavelengths, resulting in high RGB distance and low J_{SC}, due to its high reflection in the NIR region.

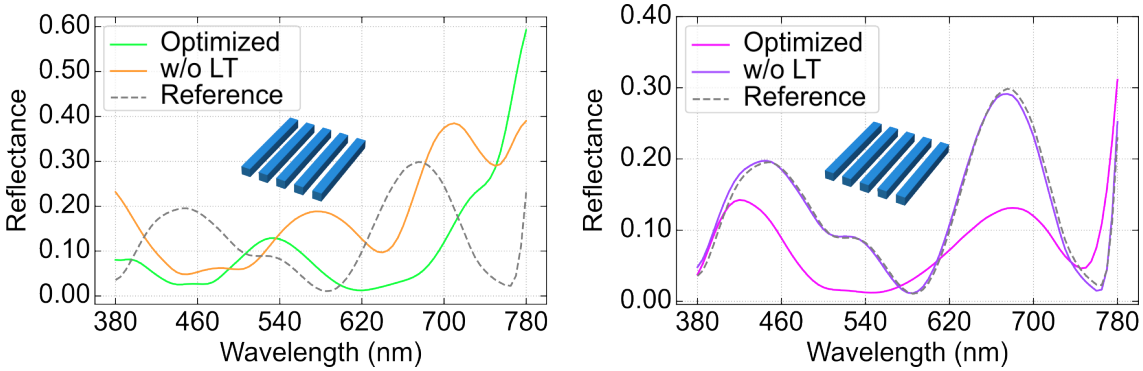


Figure B.7: Reflection spectra attained for optimal solar cells with linear gratings, with and without LT features, for green (left plot) and magenta (right plot), and respective reference spectrum. The solar cell colours were applied to each corresponding lines.

I Material data

This section provides the material information, namely the refractive indices and extinction coefficients, used in this work, in Figure I.1.

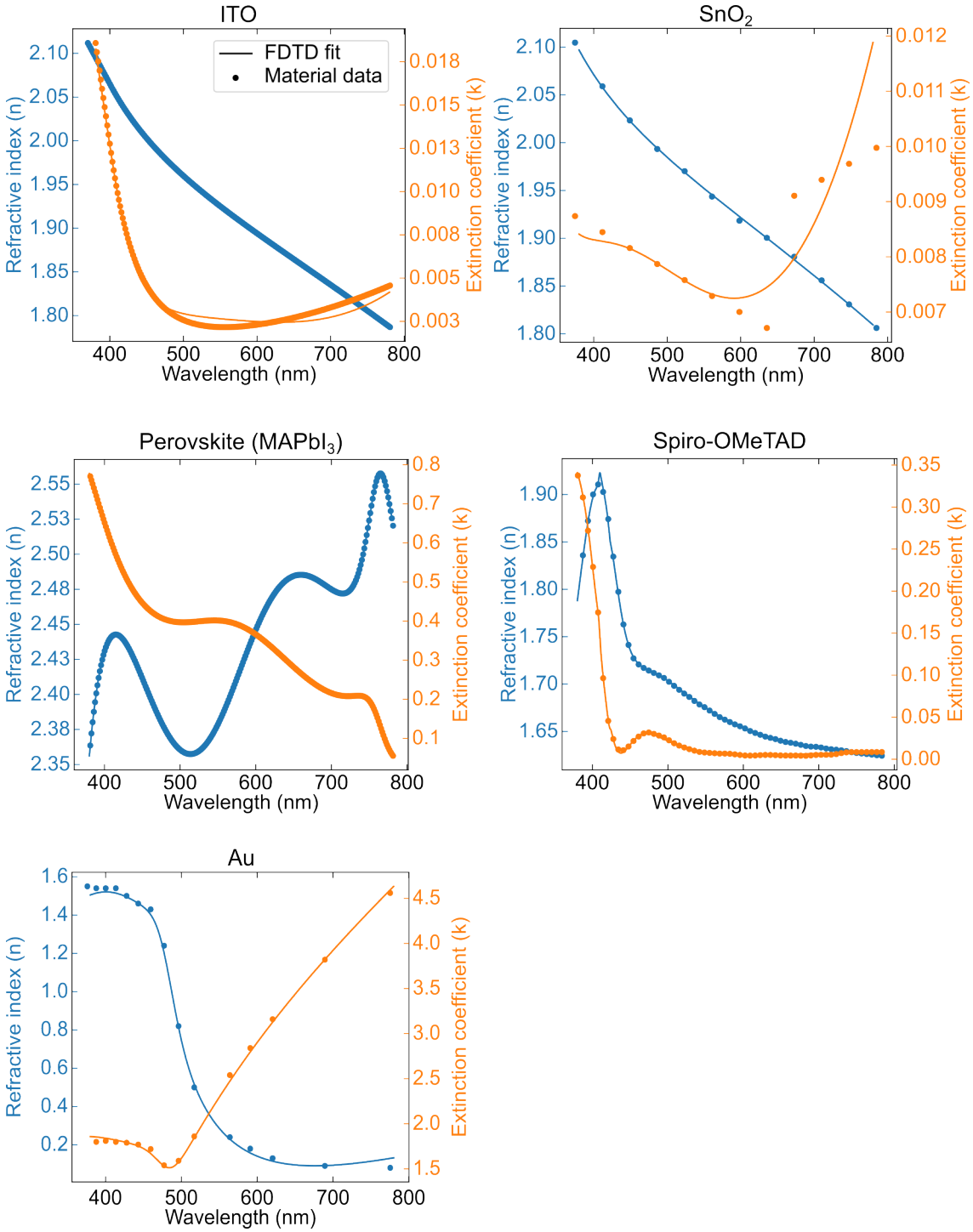


Figure I.1: Refractive index, real (n) and imaginary (k) components used to simulate the materials in the FDTD solver. Data obtained from [42].

II FDTD physics solver

The FDTD method solves Maxwell's curl equations on a mesh, which contains the material of interest, and computes the electric and magnetic fields at certain grid spatial points, at specific time stamps. Maxwell's curl equations (Equations (II.1) and (II.2)) represent how a time-varying magnetic/electric field can induce a curling electric/magnetic field, respectively, or, in a different perspective, how the curling electric/magnetic field can induce a time-varying magnetic/electric field. [32]

$$\nabla \times \vec{E} = -\frac{\partial \vec{B}}{\partial t} = -\mu \frac{\partial \vec{H}}{\partial t} \Longrightarrow \frac{\partial \vec{H}}{\partial t} = -\frac{1}{\mu} \nabla \times \vec{E} \tag{II.1}$$

$$\nabla \times \vec{H} = \frac{\partial \vec{D}}{\partial t} = \varepsilon \frac{\partial \vec{E}}{\partial t} \Longrightarrow \frac{\partial \vec{E}}{\partial t} = \frac{1}{\varepsilon} \nabla \times \vec{H} \tag{II.2}$$

In Equations (II.1) and (II.2), $\vec{E}$ and $\vec{H}$ are the symbols used for electric and magnetic fields, $\vec{D}$ and $\vec{B}$ are the electric and magnetic flux density, respectively, ε is the permittivity of the material and μ is the permeability of the material.

The discretization of the fields in time, by approximating the derivatives in finite time intervals, results in the finite-difference approximation equations. The propagation of the electric and magnetic fields throughout time is described by Equations (II.3) and (II.4), respectively. This is only possible because the FDTD algorithm provides a way to obtain the future fields from the past fields. [32]

$$\frac{\vec{H}\left(t + \frac{\Delta t}{2}\right) - \vec{H}\left(t - \frac{\Delta t}{2}\right)}{\Delta t} = -\frac{1}{\mu} \nabla \times \vec{E}\,(t) \tag{II.3}$$

$$\frac{\vec{E}\,(t + \Delta t) - \vec{E}\,(t)}{\Delta t} = \frac{1}{\varepsilon} \nabla \times \vec{H}\left(t + \frac{\Delta t}{2}\right) \tag{II.4}$$

Due to the FDTD algorithm methodology, explained in due course, the magnetic field from a past time stamp is attained at $t - \frac{\Delta t}{2}$, which is later updated to the electric field at the time stamp t. Similarly, the electric field is updated to a new future value of magnetic field, at the time stamp $t + \frac{\Delta t}{2}$, which updates to the electric field at $t + \Delta t$ [32]. The time propagation is clearer in Figure II.1, where the electric and magnetic field nodes, attained by the algorithm, appear distributed through space and time, in the past and future.

The last transformation of Maxwell's equations consists in isolating the future field values, resulting in the Update Equations, which are inserted into the FDTD algorithm. Equation (II.5) indicates that the electric field of the next time stamp, $t + \Delta t$, equals the electric field of the previous time stamp, t, added to a correction factor that results from the curl of the future magnetic field, at $t + \frac{\Delta t}{2}$, and the properties of the material. Equation (II.6) can be interpreted analogously. [32]

$$\vec{E}\,(t + \Delta t) = \vec{E}\,(t) + \frac{\Delta t}{\varepsilon} \nabla \times \vec{H}\left(t + \frac{\Delta t}{2}\right) \tag{II.5}$$

$$\vec{H}\left(t+\frac{\Delta t}{2}\right)=\vec{H}\left(t-\frac{\Delta t}{2}\right)-\frac{\Delta t}{\mu}\nabla\times\vec{E}\,(t) \tag{II.6}$$

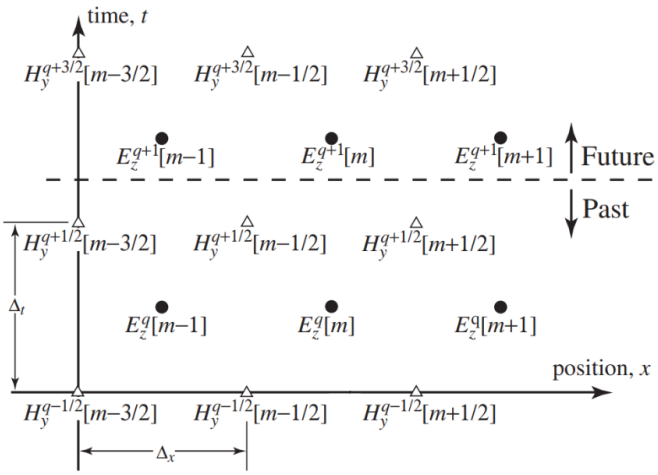


Figure II.1: Propagation of electric (circles) and magnetic (triangles) field nodes throughout space-time. The dashed line divides the nodes between future and past values. Adapted from [43].

This algorithm can be simplified to the following steps (also represented in the flowchart in Figure II.2, for clearer visualization and comprehension of the code) [32, 33]:

1. Initialize all components of the simulation – define the spacial grid and time step, set $\vec{E}=\vec{H}=0$ and define source information.

2. The FDTD engine loop updates the values of the electric and magnetic fields, in turn, by predicting the future fields, according to Equations (II.5) and (II.6).

   a) Update of the electric field from the magnetic field (Equation (II.5)).Firstly, the curly magnetic field is calculated, and then multiplied by $\frac{\Delta t}{\varepsilon}$, and added to the current value of the electric field, which results in the future value of the electric field. As the material properties may change throughout the simulation, the electric flux density is also updated for the current value of the electric field, as the permittivity, ε, changes.

   b) Update of the magnetic field from the electric field (Equation (II.6)).The curly electric field is calculated and the magnetic flux density is updated, according to changes in permeability, μ. By following Equation (II.6), this is then multiplied by $\frac{\Delta t}{\mu}$, and subtracted from the previous value of the magnetic field, which results in the future value of the magnetic field.

3. Up to this point, all values are null for all iterations, as $\vec{E}=\vec{H}=0$. It is now necessary to introduce the influence of a light source, which will alter $\vec{E}$ and $\vec{H}$ after each field update, depending on the material properties.

4. The FDTD cycle continues, revealing the propagation of the wave through a spatial and time discrete grid. The material inserted in the grid will absorb, scatter, transmit, etc., translating into a series of values of $\vec{E}$ and $\vec{H}$ through time, for each iteration. This data can then be processed and used to obtain various simulation quantities, such as transmission and reflection spectra.

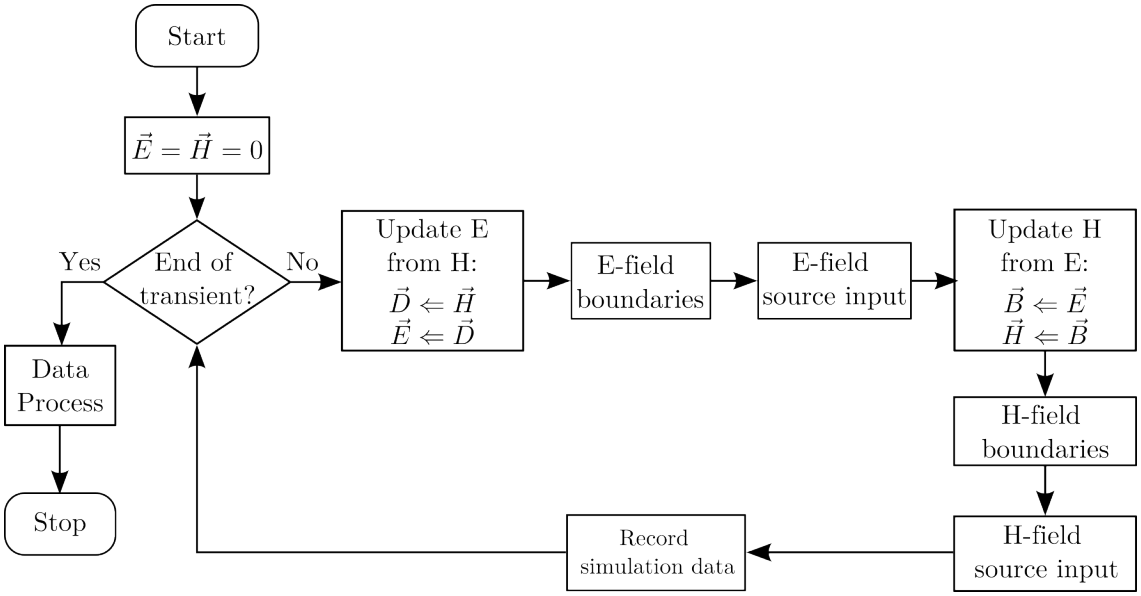


Figure II.2: FDTD flowchart - simplification of engine loop iterations, for a system with a source, grid boundaries and non-linear materials.

III CIE colour system

The human eye perceives light between the wavelengths of around 380 nm and 780 nm, via two different types of photoreceptors, rods and cones. These are responsible for processing light at low luminance environments and colour at higher luminance environments, respectively. There are three types of cone cells, responsible for colour perceptions at around blue wavelengths (S cones), green wavelengths (M cones) and red wavelengths (L cones). The responses of these cones, seen in Figure III.1(a) in normalized form, are used as a basis for all colour systems.

In order to quantify colour, CIE defined a colour-mapping function, representing the human eye's chromatic response, based on a tristimulus values that represent how much each cone is stimulated. CIE 1931 colour matching functions, $\bar{x}$, $\bar{y}$ and $\bar{z}$ (Figure III.1(b)), can mathematically describe any colour (chromaticity and luminosity) in the tristimulus diagram, by the area under the curves. Thus, tristimulus values were obtained by sweeping a power spectrum (in this case, the reflection of the cell), $P(\lambda)$, multiplying it by the colour functions, and integrating the results in wavelength, following the system of Equations (III.1). [35, 44]

$$\begin{cases} X = \int P(\lambda)\bar{x}\,(\lambda)\,\mathrm{d}\lambda \\ Y = \int P(\lambda)\bar{y}\,(\lambda)\,\mathrm{d}\lambda \\ Z = \int P(\lambda)\bar{z}\,(\lambda)\,\mathrm{d}\lambda \end{cases} \tag{III.1}$$

The next step of the algorithm consisted in normalizing the stimulus values, where the (X, Y, Z) coordinates were reduced to two values, (x, y), as Equation (III.2) exhibits, thus converting tristimulus values intro chromaticity coordinates [45]. Plotting all the possible (x, y) values results in the range of all visible chromaticities, as demonstrated in Figure III.1(c) [35]. The triangular region in the gamut represents the RGB colour space, and the respective vertices were defined as a matrix of (x, y, z) coordinates, for red, green and blue regions. The final step of the colour system algorithm consisted in dividing this matrix by the (x, y, z) vector, resulting in the (r, g, b) values, as represented in (III.3).

$$\begin{cases} x = \dfrac{X}{X+Y+Z} \\ y = \dfrac{Y}{X+Y+Z} \\ z = \dfrac{Z}{X+Y+Z} = 1 - x - y \end{cases} \tag{III.2}$$

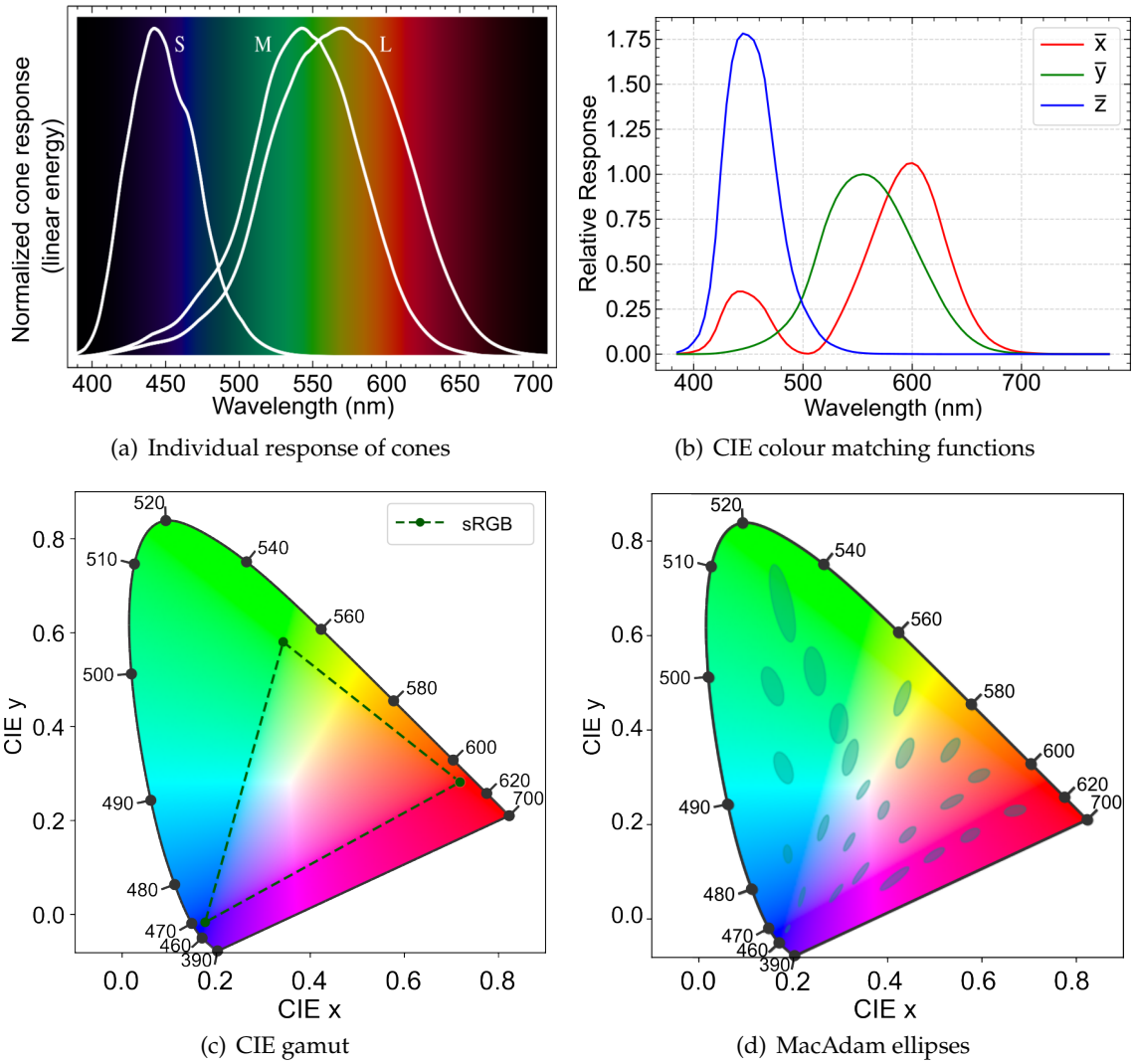
$$\begin{pmatrix} x_r & x_g & x_b \\ y_r & y_g & y_b \\ z_r & z_g & z_b \end{pmatrix} \begin{pmatrix} r \\ g \\ b \end{pmatrix} = \begin{pmatrix} x \\ y \\ z \end{pmatrix} \tag{III.3}$$

As a side note, the algorithm accounted for the possibility of (x, y) coordinates not falling within the RGB triangular region in Figure III.1(c) (the (r, g, b) vector resulted

in negative values). In this case, the colour was "desaturated", by raising the values of (r, g, b) equally until they became positive. [35]

In essence, this algorithm is capable of reading a power spectrum and determining the corresponding chromatic response, resembling the human eye sensitivity. However, by choosing to simplify the algorithm by ignoring the luminosity, it is possible that, in practice, the cell might not result in the exact same colour as predicted in simulation.

A factor to account for in the CIE 1931 system is that the human eye cannot distinguish every colour in the gamut. As shown in Figure III.1(d), the areas highlighted by ellipses enfold colours that the human eye perceives as equal (these shapes have been amplified by a factor of 10, to facilitate visualization). It is also interesting to point out that these areas present an elliptical shape, so the sensitivity in perception is not identical in CIE x and CIE y directions.



(a) Individual response of cones

(b) CIE colour matching functions

(c) CIE gamut

(d) MacAdam ellipses

Figure III.1: CIE 1931 colour space: (a) individual response of the 3 types of eye cones, responsible for the perception of wavelengths around blue (S cones), green (M cones) and red (L cones) (adapted from [46]), (b) colour matching functions, (c) chromaticity diagram for various (x, y) coordinates, with respective wavelengths shown around the gamut, in blue (the triangle represents the sRGB area) and (d) MacAdam ellipses, areas where the human eye cannot perceive the different colours (for better visualization, the ellipses are amplified by 10 times).

